Journal of Computational Physics 319 (2016) 163–199

Contents lists available at ScienceDirect

Journal of Computational Physics

www.elsevier.com/locate/jcp

A simple robust and accurate *a posteriori* sub-cell finite volume limiter for the discontinuous Galerkin method on unstructured meshes

Michael Dumbser [a,*], Raphaël Loubère [b]

[a] Department of Civil, Environmental and Mechanical Engineering, University of Trento, Via Mesiano, 77, 38123 Trento, Italy
[b] Institut de Mathématiques de Toulouse and CNRS, Université Paul Sabatier, route de Narbone, F-31062 Toulouse Cedex 9, France

ARTICLE INFO

Article history:
Received 16 September 2015
Received in revised form 3 April 2016
Accepted 2 May 2016
Available online 6 May 2016

Keywords:
Arbitrary high-order discontinuous Galerkin schemes
A posteriori sub-cell finite volume limiter
Unstructured triangular and tetrahedral meshes
Conservation laws and hyperbolic PDE with non-conservative products
Element-wise checkpointing and restarting MOOD paradigm

ABSTRACT

In this paper we propose a simple, robust and accurate nonlinear *a posteriori* stabilization of the Discontinuous Galerkin (DG) finite element method for the solution of nonlinear hyperbolic PDE systems on *unstructured* triangular and tetrahedral meshes in two and three space dimensions. This novel *a posteriori* limiter, which has been recently proposed for the simple Cartesian grid case in [62], is able to resolve discontinuities at a sub-grid scale and is substantially extended here to general unstructured simplex meshes in 2D and 3D. It can be summarized as follows:
At the beginning of each time step, an approximation of the local minimum and maximum of the discrete solution is computed for each cell, taking into account also the vertex neighbors of an element. Then, an *unlimited* discontinuous Galerkin scheme of approximation degree N is run for one time step to produce a so-called *candidate solution*. Subsequently, an *a posteriori* detection step checks the unlimited candidate solution at time t^{n+1} for positivity, absence of floating point errors and whether the discrete solution has remained within or at least very close to the bounds given by the local minimum and maximum computed in the first step. Elements that do not satisfy all the previously mentioned detection criteria are flagged as troubled cells. For these troubled cells, the candidate solution is *discarded* as inappropriate and consequently needs to be *recomputed*. Within these troubled cells the old discrete solution at the previous time t^n is scattered onto small sub-cells ($N_s = 2N + 1$ sub-cells per element edge), in order to obtain a set of sub-cell averages at time t^n. Then, a more robust second order TVD finite volume scheme is applied to update the sub-cell averages within the troubled DG cells from time t^n to time t^{n+1}. The new sub-grid data at time t^{n+1} are finally gathered back into a valid cell-centered DG polynomial of degree N by using a classical conservative and higher order accurate finite volume reconstruction technique.
Consequently, if the number N_s is sufficiently large ($N_s \geq N + 1$), the subscale resolution capability of the DG scheme is fully maintained, while preserving at the same time an essentially non-oscillatory behavior of the solution at discontinuities. Many standard DG limiters only *adjust* the discrete solution in troubled cells, based on the limiting of higher order moments or by applying a nonlinear WENO/HWENO *reconstruction* on the data at the new time t^{n+1}. Instead, our new DG limiter entirely *recomputes* the troubled cells by solving the governing PDE system again starting from valid data at the old time level t^n, but using this time a more robust scheme on the sub-grid level. In other words, the piecewise polynomials produced by the new limiter are the result of a more robust solution of the PDE system itself, while most standard DG limiters are simply based on a

* Corresponding author.
E-mail addresses: michael.dumbser@unitn.it (M. Dumbser), raphael.loubere@math.univ-toulouse.fr (R. Loubère).

http://dx.doi.org/10.1016/j.jcp.2016.05.002

mere nonlinear data post-processing of the discrete solution. Technically speaking, the new method corresponds to an element-wise *checkpointing* and *restarting* of the solver, using a lower order scheme on the sub-grid. As a result, the present DG limiter is even able to *cure* floating point errors like NaN values that have occurred after divisions by zero or after the computation of roots from negative numbers. This is a unique feature of our new algorithm among existing DG limiters.

The new *a posteriori* sub-cell stabilization approach is developed within a high order accurate one-step ADER-DG framework on multidimensional unstructured meshes for hyperbolic systems of conservation laws as well as for hyperbolic PDE with non-conservative products. The method is applied to the Euler equations of compressible gas dynamics, to the ideal magneto-hydrodynamics equations (MHD) as well as to the seven-equation Baer–Nunziato model of compressible multi-phase flows. A large set of standard test problems is solved in order to assess the accuracy and robustness of the new limiter.

1. Introduction

The Discontinuous Galerkin (DG) finite element method was introduced for the first time in a seminal paper by Reed and Hill [117] in the context of linear scalar neutron transport equations. A well-known series of papers by Cockburn and Shu [33,32,31,29,34] has subsequently established a solid background for its application to general nonlinear systems of hyperbolic conservation laws in one and multiple space dimensions. A remarkable property of the DG method is that it satisfies a local cell entropy inequality even for higher orders of accuracy, provided that the numerical flux used at the element boundaries is a monotone entropy flux. From the local cell entropy property, it is trivial to prove that the DG method is stable in L_2 norm, see the paper by Jiang and Shu [81] for the nonlinear scalar case and its subsequent extensions to nonlinear systems [18,77]. However, despite this very interesting nonlinear stability property, the DG method is still a linear scheme in the sense of Godunov [71], hence even the DG method needs some sort of nonlinear limiting to avoid the spurious oscillations, i.e. Gibbs phenomenon, in the presence of discontinuities.

In most cases, the DG method is used in the so-called method of lines (MOL) framework, i.e. first only a spatial discretization is carried out, while time is still kept continuous. The resulting *semi-discrete* scheme leads to a nonlinear ODE system, which is then typically advanced in time via explicit TVD Runge–Kutta schemes, see the work of Shu & Osher [125,126] and Gottlieb & Shu [72]. The resulting method is consequently called Runge–Kutta DG (RKDG) scheme. For an overview of existing DG schemes see [30,35,74]. However, explicit RKDG schemes suffer from a very severe time step restriction, where the maximum admissible Courant number typically scales as approximately $1/(2N+1)$, if N denotes the polynomial degree of the approximation of the DG scheme. Alternative explicit time discretizations for DG methods have been proposed, which lead to so-called *fully-discrete* one-step schemes that do not require any intermediate Runge–Kutta stages. The resulting methods are the Lax–Wendroff DG method [112], the ADER-DG[1] method [129,56,47] and the STE-DG method [98,70]. For a detailed comparison of different explicit one-step time discretizations of DG schemes see [69]. Unfortunately, all the fully-discrete DG schemes mentioned before suffer from an even more severe stability restriction than the RKDG method. A space-time discontinuous Galerkin scheme has been introduced by Van der Vegt et al. in [135,136,92] and has subsequently been analyzed by Feistauer et al. in [66,27]. The space-time DG method is theoretically of arbitrary high order of accuracy in both space and time and is provably unconditionally stable. However, these schemes are implicit, they require the solution of a global nonlinear system for the unknown degrees of freedom, which might result difficult for big meshes, large PDE systems or for high polynomial approximation degrees. In order to reduce the complexity of globally implicit space-time DG schemes, a *local* space-time DG approach has been forwarded in [51,75,47]. This method is only locally implicit and therefore requires only the solution of small nonlinear systems that can be easily handled element-wise. The local space-time DG approach leads again to an explicit scheme that is subject to a CFL condition on the time step for explicit one-step DG schemes, but it replaces the cumbersome Cauchy–Kovalewski procedure that has been previously used in Lax–Wendroff DG, ADER-DG and STE-DG schemes.

There is a vast literature on limiters for the discontinuous Galerkin finite element method, and only a very short and non-exhaustive review on this topic can be given here. A common point of many DG limiters is to apply first an unlimited DG scheme and to evolve the discrete solution to the new time level. Then, an appropriate indicator detects so-called *troubled cells*, i.e. those elements of the computational domain that need limiting, see for example [84,94,97,138]. For detected troubled cells, the degrees of freedom of the discrete solution are then typically *modified* by some sort of nonlinear *postprocessing* after each time step, e.g. by a TVD/TVB limiting [33,32,31,29], or via a nonlinear ENO/WENO/HWENO reconstruction [115,113,114,6,146,87,86,148,147,83,76,6] or by a so-called moment limiting [116,2,94,97,101,141,42–44].

[1] ADER stands for **a**rbitrary high order **der**ivatives. The method was proposed by Toro and Titarev in [134] for the approximate solution of the generalized Riemann problem that consists of piecewise smooth initial data separated by a discontinuity.

A completely different and historically much older approach to limiting numerical schemes for nonlinear hyperbolic systems is the artificial viscosity (AV) method. It dates back to von Neumann and Richtmyer [107], who developed the AV approach in the 1940's at Los Alamos National Laboratory. The basic idea of AV techniques is to add a purely artificial dissipative mechanism to the difference equations. The dissipation should be strong enough so that the shock transition would become a smooth one, hence spreading the shock over a small number of cells. In the context of discontinuous Galerkin finite element schemes, the artificial viscosity concept has become popular again, and the reader is referred to [118,110,17,99,36,45] for details.

Recently, a new concept to the problem of limiting has been proposed in the finite volume context, the so-called Multi-dimensional Optimal Order Detection (MOOD) approach. The key idea is to run first a spatially high order accurate but *unlimited* finite volume scheme. This step produces a so-called *candidate solution*. Then, the validity of this candidate solution is tested *a posteriori* against a set of predefined *admissibility criteria*. The cells which pass all these criteria are marked as 'acceptable', while those who fail to pass an admissibility criterion are marked as 'troubled'. The troubled cells and their neighbors are subsequently *recomputed* locally using a polynomial reconstruction of lower degree. In that way, a new candidate solution is obtained, which is then again tested against the admissibility criteria and, where necessary, the polynomial degree of the reconstruction is locally reduced again. In the worst case, a cell is updated with a robust and stable first order accurate Godunov-type finite volume scheme, which is supposed to produce always a valid (monotone and positivity-preserving) solution under CFL condition. For more details about the MOOD paradigm in the finite volume context, the reader is referred to [28,40,41,100]. There is an obvious link between the MOOD concept in the finite volume framework and the typical strategy adopted in a classical DG limiter: in both approaches first a candidate solution is computed using a high order accurate *unlimited* scheme. Then, troubled cells are detected based on some criteria and the discrete solution is corrected. However, there is a fundamental difference: within a typical DG limiter the candidate solution is only *postprocessed*, either by a nonlinear TVD/TVB or an ENO/WENO/HWENO reconstruction or by some other sort of moment limiting. Classical DG limiters furthermore work only on one time level in order to detect and correct troubled cells. The MOOD approach on the other hand uses *two* time levels (the old one and the current one) for the detection of troubled cells. Second, the MOOD method really *discards* the candidate solution and *recomputes* a new one by starting again from the discrete solution at the old time level and by using a different and more robust numerical scheme. In technical terms this means that the code applies in the troubled cells in each time step an element-wise *checkpointing* and *restarting*, invoking at the restart a different scheme that is more adequate to handle shock waves and other nonlinear phenomena. The detection being based on two time levels and the local checkpointing and restarting makes the MOOD method [28,40,41,100] an *a posteriori* detection and correction approach.

Very recently, a high order one-step ADER Discontinuous Galerkin (DG) scheme that has been stabilized with a novel *a posteriori* sub-cell finite volume limiter for hyperbolic systems of conservation laws has been developed on simple uniform as well as on adaptive Cartesian grids in [62,143,142]. However, in more complex situations that typically arise in engineering and geo-sciences, the use of an unstructured mesh may be mandatory due to the geometrical complexity of the computational domain. For this reason, it is the goal of this paper to extend the *a posteriori* sub-cell finite volume limiter originally developed in [62] to the case of unstructured meshes in two and three space dimensions, as well as to the case of non-conservative hyperbolic PDE. We will furthermore illustrate that the new sub-cell limiter is able to maintain the extraordinary resolution capabilities of the DG method not only in regions where the solution of the PDE is smooth, but also in the vicinity of steep fronts, shock waves and other discontinuities. With this new approach, it is indeed possible to resolve a shock wave or a contact discontinuity well *within* one single cell. For alternative subcell limiters in the context of high order discontinuous Galerkin finite element schemes, the reader is also referred to the work of Huerta et al. [80,23], Sonntag and Munz [128], Fechter and Munz [65] and Meister and Ortleb [103]. However, to the knowledge of the authors, none of the above mentioned methods has ever been extended and applied to high order DG schemes on unstructured tetrahedral meshes in three space dimensions.

The rest of the paper is organized as follows. In Section 2 we describe the governing PDE systems to be discretized in this article, as well as the unlimited ADER-DG scheme. In the following Section 3 we present the *a posteriori* detection of problematic cells along with the sub-cell finite volume scheme that is used to *recompute* the discrete solution in troubled cells at the aid of a more robust scheme that is used at the sub-grid level. Section 4 is entirely dedicated to the numerical experiments which have been carried out. A large set of test problems has been simulated for three important PDE systems, namely the Euler equations of compressible gas dynamics, the ideal magnetohydrodynamics equations (MHD) and the seven-equation Baer–Nunziato model of compressible multi-phase flows. Some test problems involve smooth solutions in order to check, whether the designed high order of accuracy of our new method is achieved. Other tests contain discontinuities in order to assess the robustness of our method. We show in these examples that the sub-scale resolution capability of the DG method is properly maintained by the new *a posteriori* stabilization technique. The paper closes with some concluding remarks given in Section 5.

2. Unlimited one-step ADER-DG scheme

In this paper we will consider general non-linear systems of hyperbolic PDE, which can be expressed in the following compact form:

$$\frac{\partial \mathbf{Q}}{\partial t} + \nabla \cdot \mathbf{F}(\mathbf{Q}) + \mathbf{B}(\mathbf{Q}) \cdot \nabla \mathbf{Q} = \mathbf{0}, \tag{1}$$

where $\mathbf{Q} = \mathbf{Q}(\mathbf{x}, t) \in \mathbb{R}^{\nu}$ is the state vector; $\mathbf{x} = (x, y, z) \in \Omega$ is the vector of spatial coordinates and Ω denotes the computational domain; $\mathbf{F}(\mathbf{Q}) = (\mathbf{f}, \mathbf{g}, \mathbf{h})$ is the nonlinear flux tensor that contains the conservative part of the PDE system and $\mathbf{B}(\mathbf{Q}) \cdot \nabla \mathbf{Q}$ is a genuinely non-conservative term. When written in quasilinear form, the system (1) becomes

$$\frac{\partial \mathbf{Q}}{\partial t} + \mathbf{A}(\mathbf{Q}) \cdot \nabla \mathbf{Q} = \mathbf{0}, \tag{2}$$

where the matrix $\mathbf{A}(\mathbf{Q}) = \partial \mathbf{F}(\mathbf{Q}) / \partial \mathbf{Q} + \mathbf{B}(\mathbf{Q})$ contains both, the Jacobian of the conservative flux, as well as the non-conservative product. The system (2) is hyperbolic if for any unit-normal vector $\mathbf{n}$ with $\|\mathbf{n}\| = 1$ the matrix $\mathbf{A}_n = \mathbf{A}(\mathbf{Q}) \cdot \mathbf{n} = \mathbf{R}_n(\mathbf{Q})\, \mathbf{\Lambda}_n(\mathbf{Q})\, \mathbf{R}_n^{-1}(\mathbf{Q})$ is diagonalizable with a diagonal matrix $\mathbf{\Lambda}_n = \mathrm{diag}(\lambda_1, \lambda_2, \ldots, \lambda_i, \ldots, \lambda_{\nu})$ of real eigenvalues λ_i and a complete set of linearly independent right eigenvectors $\mathbf{R}_n$.

The PDE system (1) is solved at the aid of a high order one-step ADER-DG method [112,47,50], which provides at the same time high order of accuracy in both space and time in one single step, without the need of any intermediate Runge–Kutta stages. The construction of fully-discrete high order one-step schemes is typical of the ADER approach, which was forwarded by Toro and Titarev in the finite volume context, see [134,131,132]. The scheme is written under the form of a one-step predictor corrector method [69], where the predictor step solves (1) within each element *in the small* (see also [73]) by means of an element-local space-time discontinuous Galerkin scheme. The corrector step is obtained by directly integrating a weak form of the governing PDE in time at the aid of the predictor. In the following we only summarize the main steps, while for more details the reader is referred to [47,60,75,69,16].

2.1. Data representation and spatial discretization

The computational domain Ω is discretized by an unstructured mesh composed of conforming simplex elements denoted by T_i, where the index i ranges from 1 to the total number of elements N_E. The T_i are triangles in two space dimensions and tetrahedra in the three-dimensional case. The union of all elements represents the triangulation (tetrahedrization) of the computational domain,

$$\mathcal{T}_{\Omega} = \bigcup_{i=1}^{N_E} T_i, \tag{3}$$

and is also called the *main grid* in the following. We will further denote the cell volume by $|T_i| = \int_{T_i} d\mathbf{x}$. The discrete solution of PDE (1) is denoted by $\mathbf{u}_h(\mathbf{x}, t^n) \in \mathcal{U}_h$ and is represented by piecewise polynomials of maximum degree $N \geq 0$. Within each cell T_i we have

$$\mathbf{u}_h(\mathbf{x}, t^n) = \sum_{l}^{\mathcal{M}} \Phi_l(\mathbf{x}) \hat{\mathbf{u}}_{l,i}^n := \Phi_l(\mathbf{x})\, \hat{\mathbf{u}}_{l,i}^n, \quad \mathbf{x} \in T_i, \tag{4}$$

where we have introduced the classical Einstein summation convention over two repeated indices. The approximation space $\mathcal{U}_h$ of piecewise polynomials up to degree N is spanned by the basis functions $\Phi_l = \Phi_l(\mathbf{x})$. Throughout this paper we use the orthogonal Dubiner-type basis for simplex elements, which is a so-called *modal basis*, detailed in [46,89,30]. The symbol $\mathcal{M}$ denotes the number of degrees of freedom per element and is given by $\mathcal{M} = (N+1)(N+2)/2$ in two space dimensions and by $\mathcal{M} = (N+1)(N+2)(N+3)/6$ in three space dimensions, respectively. The basis functions are conveniently defined in a reference simplex element T_e, defined by the nodes $\mathbf{\Xi}_1 = (0, 0)$, $\mathbf{\Xi}_2 = (1, 0)$ and $\mathbf{\Xi}_3 = (0, 1)$ in the two-dimensional case and by $\mathbf{\Xi}_1 = (0, 0, 0)$, $\mathbf{\Xi}_2 = (1, 0, 0)$, $\mathbf{\Xi}_3 = (0, 1, 0)$ and $\mathbf{\Xi}_4 = (0, 0, 1)$ in the three-dimensional case, respectively. The vertices that define T_i in the physical coordinate system are denoted by $\mathbf{X}_1$, $\mathbf{X}_2$, $\mathbf{X}_3$ and $\mathbf{X}_4$, respectively. The mapping from the reference element to the physical element is then given in the general 3D case by the simple linear transformation

$$\mathbf{x} = \mathbf{X}_1 + (\mathbf{X}_2 - \mathbf{X}_1)\, \xi + (\mathbf{X}_3 - \mathbf{X}_1)\, \eta + (\mathbf{X}_4 - \mathbf{X}_1)\, \zeta, \tag{5}$$

where $\boldsymbol{\xi} = (\xi, \eta, \zeta)$ is the coordinate vector in the reference system and from which the 2D case can be obtained by simply setting $\zeta = 0$.

2.2. Local space-time predictor

The discrete solution $\mathbf{u}_h(\mathbf{x}, t^n)$ is now evolved in time according to an element-local weak formulation of the governing PDE in space-time, see [51,47,75,60,69,16]. The local space-time Galerkin method is only used for the construction of an element-local predictor solution of the PDE *in the small*, hence neglecting the influence of neighbor elements. This predictor solution will subsequently be inserted into the corrector step described in the next section, which then provides the appropriate coupling between neighbor elements via a numerical flux function (Riemann solver) and a path-conservative jump term for the discretization of the non-conservative product. To simplify notation, we define

$$\langle f, g \rangle = \int_{t^n}^{t^{n+1}} \int_{T_i} f(\mathbf{x},t) g(\mathbf{x},t)\, d\mathbf{x}\, dt, \qquad [f, g]^t = \int_{T_i} f(\mathbf{x},t) g(\mathbf{x},t)\, d\mathbf{x}, \tag{6}$$

which denote the scalar products of two functions f and g over the space-time element $T_i \times \left[t^n; t^{n+1}\right]$ and over the spatial element T_i at time t, respectively. Within the local space-time predictor, the discrete solution of equation (1) is denoted by $\mathbf{q}_h = \mathbf{q}_h(\mathbf{x},t)$. We then multiply (1) with a space-time test function $\theta_k = \theta_k(\mathbf{x},t)$ and subsequently integrate over the space-time control volume $T_i \times \left[t^n; t^{n+1}\right]$. Inserting $\mathbf{q}_h$, the following weak formulation of the PDE is obtained:

$$\left\langle \theta_k, \frac{\partial \mathbf{q}_h}{\partial t} \right\rangle + \langle \theta_k, \nabla \cdot \mathbf{F}(\mathbf{q}_h) + \mathbf{B}(\mathbf{q}_h) \cdot \nabla \mathbf{q}_h \rangle = 0. \tag{7}$$

The discrete representation of $\mathbf{q}_h$ in element $T_i \times [t^n, t^{n+1}]$ is assumed to have the following form

$$\mathbf{q}_h = \mathbf{q}_h(\mathbf{x},t) = \sum_l \theta_l(\mathbf{x},t) \hat{\mathbf{q}}_{l,i}^n := \theta_l \hat{\mathbf{q}}_{l,i}^n, \tag{8}$$

where $\theta_l(\mathbf{x},t)$ is a space-time basis function of maximum degree N. For the basis functions θ_l we use the nodal basis given in [47], that consists in the Lagrange interpolation polynomials passing through a set of pre-defined space-time nodes. In principle, any basis can be used. However, the use of a nodal basis is computationally more efficient compared with a modal basis. After integration by parts in time of the first term, eqn. (7) reads

$$[\theta_k, \mathbf{q}_h]^{t^{n+1}} - \left[\theta_k, \mathbf{u}_h(\mathbf{x}, t^n)\right]^{t^n} - \left\langle \frac{\partial}{\partial t}\theta_k, \mathbf{q}_h \right\rangle + \langle \theta_k, \nabla \cdot \mathbf{F}(\mathbf{q}_h) + \mathbf{B}(\mathbf{q}_h) \cdot \nabla \mathbf{q}_h \rangle = 0. \tag{9}$$

Note that the high order polynomial data representation of the DG scheme $\mathbf{u}_h(\mathbf{x}, t^n)$ is taken into account in (9) as initial condition of the element-local Cauchy problem in the small in a weak sense by the term $[\theta_k, \mathbf{u}_h(\mathbf{x}, t^n)]^{t^n}$. This corresponds to the choice of a numerical flux in time direction, which is nothing else than *upwinding in time*, according to the causality principle. Note that due to the DG approximation in space-time, we may have $\mathbf{q}_h(\mathbf{x}, t^n) \neq \mathbf{u}_h(\mathbf{x}, t^n)$ in general, hence the choice of a numerical flux in time direction is necessary. Note further that in (9) we have *not* used integration by parts in space, nor any other coupling to spatial neighbor elements. The integrals appearing in the weak form (9), as well as the space-time test and basis functions involved are conveniently written by making use of a space-time reference element $T_e \times [0; 1]$.

The solution of (9) yields the unknown space-time degrees of freedom $\hat{\mathbf{q}}_{l,i}^n$ for each space-time element $T_i \times [t^n; t^{n+1}]$ and is easily achieved with a fast converging iterative scheme, see [47,75,60] for more details. The above space-time Galerkin predictor has replaced the cumbersome Cauchy–Kovalewski procedure that has been initially employed in the original version of ADER finite volume and ADER discontinuous Galerkin schemes [123,130,134,131,56,129,55].

2.3. Fully discrete one-step ADER-DG scheme

At the aid of the local space-time predictor $\mathbf{q}_h$, a fully discrete one-step ADER-DG scheme can now be simply obtained by multiplication of the governing PDE system (1) by test functions $\Phi_k \in \mathcal{U}_h$, which are identical with the spatial basis functions, and subsequent integration over the space-time control volume $T_i \times [t^n; t^{n+1}]$. Due to the presence of non-conservative products, the jumps of $\mathbf{q}_h$ across element boundaries are taken into account in the framework of path-conservative schemes put forward by Castro and Parés in the finite volume context [25,109] and subsequently extended to DG schemes in [119] and [50,52], where also a generalization to the unified $P_N P_M$ framework has been provided. All these approaches are based on the theory of Dal Maso, Le Floch and Murat [102], which gives a definition of weak solutions in the context of non-conservative hyperbolic PDE. For open problems concerning path-conservative schemes, the reader is referred to [26] and [1].

If $\mathbf{n}$ is the outward pointing unit normal vector on the surface ∂T_i of element T_i and the path-conservative jump term in normal direction is denoted by $\mathcal{D}^-\left(\mathbf{q}_h^-, \mathbf{q}_h^+\right) \cdot \mathbf{n}$, which is a function of the left and right boundary-extrapolated data, $\mathbf{q}_h^-$ and $\mathbf{q}_h^+$, respectively, then we obtain the following path-conservative one-step ADER Discontinuous Galerkin (ADER-DG) scheme, see [50]:

$$\left(\int_{T_i} \Phi_k \Phi_l d\mathbf{x} \right) \left(\hat{\mathbf{u}}_l^{n+1} - \hat{\mathbf{u}}_l^n \right) + \int_{t^n}^{t^{n+1}} \int_{\partial T_i} \Phi_k \mathcal{D}^-\left(\mathbf{q}_h^-, \mathbf{q}_h^+\right) \cdot \mathbf{n}\, dS dt + \int_{t^n}^{t^{n+1}} \int_{T_i \setminus \partial T_i} \Phi_k \left(\nabla \cdot \mathbf{F}(\mathbf{q}_h) + \mathbf{B}(\mathbf{q}_h) \cdot \nabla \mathbf{q}_h\right) d\mathbf{x} dt = 0. \tag{10}$$

The element mass matrix appears in the first integral of (10), the second term accounts for the jump in the discrete solution at element boundaries and the third term takes into account the smooth part of the non-conservative product. In general we

use the simple Rusanov (local Lax Friedrichs) method [120], or the more sophisticated Osher-type scheme recently proposed in [58,59,24] as approximate Riemann solver at the element boundaries, although any other kind of Riemann solver could be also considered, see [133] for an overview of state-of-the-art Riemann solvers. At that point we would also like to point out the new general reformulation of the HLLEM Riemann solver of Einfeldt and Munz [63,64], within the setting of path-conservative schemes recently forwarded in [48].

The Rusanov jump term reads

$$\mathcal{D}^-\left(\mathbf{q}_h^-,\mathbf{q}_h^+\right)\cdot\mathbf{n}=\frac{1}{2}\left(\mathbf{F}(\mathbf{q}_h^+)-\mathbf{F}(\mathbf{q}_h^-)\right)\cdot\mathbf{n}+\frac{1}{2}\left(\tilde{\mathbf{B}}\cdot\mathbf{n}-s_{\max}\mathbf{I}\right)\left(\mathbf{q}_h^+-\mathbf{q}_h^-\right), \tag{11}$$

with the maximum signal speed at the element interface $s_{\max}=\max\left(\left|\mathbf{\Lambda}(\mathbf{q}_h^+)\right|,\left|\mathbf{\Lambda}(\mathbf{q}_h^-)\right|\right)$ and the matrix $\tilde{\mathbf{B}}\cdot\mathbf{n}$ given by the following path-integral along a straight line segment path ψ:

$$\tilde{\mathbf{B}}\cdot\mathbf{n}=\int_0^1\mathbf{B}\left(\psi(\mathbf{q}_h^-,\mathbf{q}_h^+,s)\cdot\mathbf{n}\,ds,\qquad\psi\left(\mathbf{q}_h^-,\mathbf{q}_h^+,s\right)=\mathbf{q}_h^-+s\left(\mathbf{q}_h^+-\mathbf{q}_h^-\right).\right. \tag{12}$$

The path-conservative Osher-type Riemann solver based on the same straight line segment path ψ reads

$$\mathcal{D}^-\left(\mathbf{q}_h^-,\mathbf{q}_h^+\right)\cdot\mathbf{n}=\frac{1}{2}\left(\mathbf{F}(\mathbf{q}_h^+)-\mathbf{F}(\mathbf{q}_h^-)\right)\cdot\mathbf{n}+\frac{1}{2}\left(\int_0^1\left(\mathbf{B}\left(\psi(\mathbf{q}_h^-,\mathbf{q}_h^+,s)\cdot\mathbf{n}-\left|\mathbf{A}\left(\psi(\mathbf{q}_h^-,\mathbf{q}_h^+,s)\cdot\mathbf{n}\right|\right)ds\right)\right)\left(\mathbf{q}_h^+-\mathbf{q}_h^-\right), \tag{13}$$

with the usual definition $|\mathbf{A}|=\mathbf{R}|\mathbf{\Lambda}|\mathbf{R}^{-1}$. According to the suggestions made in [50,52,58,24,59], the path-integrals can be conveniently evaluated numerically by the use of a classical Gauss–Legendre quadrature formula on the unit interval $[0;1]$. For an alternative choice of the path, see [104,105].

This completes the brief description of the *unlimited* ADER-DG scheme used for the discretization of the governing PDE system (1).

3. The *a posteriori* sub-cell finite volume limiter on unstructured simplex meshes

The discrete representation of the solution within a general simplex element T_i is denoted by $\mathbf{u}_h(\mathbf{x},t^n)$ at the beginning of a time step. At the next time level t^{n+1} we first calculate a so-called *candidate* solution, denoted as $\mathbf{u}_h^*(\mathbf{x},t^{n+1})$, which results from the *unlimited* ADER-DG scheme (10) described in the previous section. From these data the *a posteriori* sub-cell limiter acts in two stages [62]:

- *Detect* troubled cells in the candidate solution, that is at t^{n+1}, which are not acceptable according to some user-defined or developer-given physical and numerical detection criteria. This step is similar to existing troubled zones indicators used in classical state-of-the-art DG limiters [29,34,84].
- *Discard* the candidate DG solution in these troubled cells and *recompute* the discrete solution *locally*, starting again from the previous time level t^n, but this time using a more robust Finite Volume (FV) scheme operating on a sufficiently large number of sub-cells, as to conserve the intrinsic subcell resolution capability of a high order DG scheme. The feature that the solution is locally *recomputed* by starting again from a valid discrete solution at the previous time level is *radically different* from existing classical DG limiters.

This stabilization technology is based on two salient remarks:

- The **subscale resolution** capability of the DG method that is intrinsically embedded in its piecewise high order polynomial data representation should not be destroyed by a limiter. In other words: a limiter should not act on the characteristic length scale h of the main grid, but on a length scale that is less than $h/(N+1)$.
  As an illustration, in 1D, a $\mathbb{P}_N$ polynomial has $N+1$ degrees of freedom. These degrees of freedom can be either the $N+1$ coefficients needed to develop $\mathbf{u}_h$ in a polynomial basis up to degree N, or, equivalently, the projection of $\mathbf{u}_h$ onto a set of N_s finite volume sub-cells. If the number of sub-cells is large enough ($N_s\geq N+1$) we can retrieve the DG polynomial back from these finite volume data via a standard reconstruction operator. Consequently, the data contained inside a polynomial of degree N can be also alternatively represented by a set of sub-cell averages on a sub-grid. Concerning the information content, it is therefore equivalent to substitute DG polynomials on elements of the main grid by FV cell averages on the sub-cells. The gain is that finite volume schemes are notoriously much simpler to stabilize at strong shocks than DG schemes, by means of a vast number of well established techniques: slope and flux limiters, ENO/WENO reconstruction, the MOOD approach [28,40,41] or, more drastically, by simply employing a first order Godunov-type finite volume scheme with its large numerical viscosity.

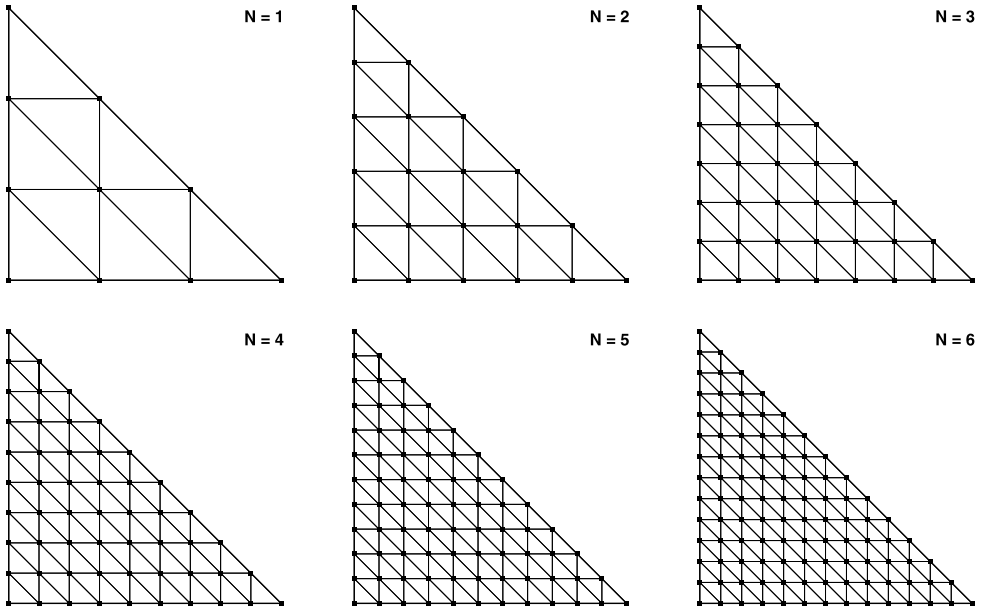

Fig. 1. Sub-grid used for the *a posteriori* sub-cell finite volume limiter of DG schemes on triangles in 2D from $\mathbb{P}1$ to $\mathbb{P}6$.

- The **observation** of a problematic numerical solution in a cell is much easier than the **prediction** of its occurrence. In other words, given a computed candidate solution at t^{n+1} it is relatively easy to determine if the numerical solution fits our expectations, or, where it fails to. Contrarily, it seems more difficult to ensure that, given a solution at t^n, the numerical method will produce a valid solution after its evolution during one time step. This illustrates the difference between *a posteriori* checking the validity of a numerical solution *versus* building a numerical method which, *a priori*, ensures the validity of a solution, that is without the knowledge of any data at the future time t^{n+1}.[2]

Our DG sub-cell limiter is therefore constructed taking into account these two remarks. First, any DG polynomial on a given cell can be equivalently represented by a collection of piecewise constant finite volume data on a sub-grid of the cell and vice-versa. Second, at the end of the timestep the numerical solution of the DG scheme has to pass a set of detection tests to be considered as a valid solution. If it does not, this candidate DG solution in these so-called troubled/problematic cells is simply discarded and recomputed with a finite volume scheme acting on a sub-cell mesh of the troubled cell.

3.1. Sub-cell finite volume recomputation

3.1.1. From cell to sub-cells

Assume that cell T_i onto which a DG polynomial $\mathbf{u}_h$ is defined has been detected as problematic. Then we first pave it with a sub-grid made of $(N_s)^d$ sub-cells $S_{i,j}$, with $j = 1, \cdots, (N_s)^d$, where $N_s = 2N + 1$, see Fig. 1 for the two dimensional case and Fig. 2 for the three dimensional case, respectively. The number N_s defines into how many sub-edges an edge of the simplex element T_i is divided. This means that the characteristic length scale of the sub-grid is h/N_s, if h is the characteristic size of an element on the main grid.

The motivation for our particular choice of N_s is given in detail in [62]. The two main reasons for using $N_s = 2N + 1$ are first the quality of the resolution of discontinuities on the sub-grid and second the fact that in this way the time step condition of the finite volume scheme on the sub-grid ($\mathrm{CFL}_{\mathrm{FV}} \leq 1$) matches the one of an explicit RK-DG scheme on the main grid ($\mathrm{CFL}_{\mathrm{DG}} \leq 1/(2N+1)$). The fact that the finite volume scheme on the subgrid is run with the maximum admissible CFL number means that the phase and amplitude errors are minimized, see [57] for a detailed analysis in the case of the 1D linear scalar advection equation.

The nodes that define the sub-grid are simply given by the standard nodes of classical high order conforming finite elements on simplex meshes. On the reference element, the sub-node coordinates $\boldsymbol{\xi}$ are

$$\boldsymbol{\xi}_{k,l} = \left(\frac{k}{N_s}, \frac{l}{N_s} \right), \qquad \text{and} \qquad \boldsymbol{\xi}_{j,k,l} = \left(\frac{j}{N_s}, \frac{k}{N_s}, \frac{l}{N_s} \right), \tag{14}$$

[2] In the Online Encyclopedia of Philosophy (http://www.iep.utm.edu/apriori [85]) an article written by J.S. Baehr states that *"A priori" and "a posteriori" refer primarily to how, or on what basis, a proposition might be known. In general terms, a proposition is knowable a priori if it is knowable independently of experience, while a proposition knowable a posteriori is knowable on the basis of experience. The distinction between a priori and a posteriori knowledge thus broadly corresponds to the distinction between empirical and nonempirical knowledge.*

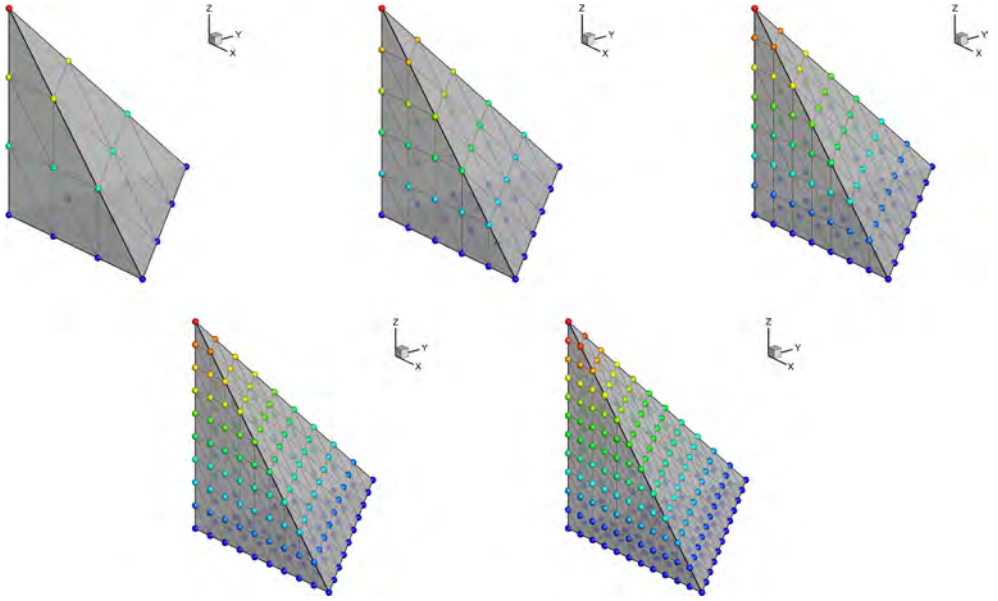

Fig. 2. Sub-grid used for the *a posteriori* sub-cell finite volume limiter of DG schemes on tetrahedra in 3D from $\mathbb{P}1$ to $\mathbb{P}5$.

for the two- and the three-dimensional case, respectively, with $0 \le l \le N_s$, $0 \le k \le N_s - l$ and $0 \le j \le N_s - l - k$. We therefore have $\mathcal{M}_s = (N_s+1)(N_s+2)/2$ subnodes in 2D and $\mathcal{M}_s = (N_s+1)(N_s+2)(N_s+3)/6$ subnodes in 3D.

The connectivity for the sub-grid on the triangle is trivial. There are only two *types* of sub-triangles, the upward pointing sub-triangles $S^u_{k,l}$ and the downward pointing sub-triangles $S^d_{k,l}$, whose connectivity is given by the formulae

$$S^u_{k,l} = (\boldsymbol{\xi}_{k,l}, \boldsymbol{\xi}_{k+1,l}, \boldsymbol{\xi}_{k,l+1}), \qquad S^d_{k,l} = (\boldsymbol{\xi}_{k+1,l+1}, \boldsymbol{\xi}_{k,l+1}, \boldsymbol{\xi}_{k+1,l}). \tag{15}$$

In 3D, the connectivity is slightly more complex. There are again upward-pointing sub-tetrahedra $S^u_{j,k,l}$ and downward-pointing sub-tetrahedra $S^d_{j,k,l}$. However, in the 3D case there arises a set of intermediate *octahedron holes*, each of which needs to be closed by four additional types of sub-tetrahedra, namely $S^I_{j,k,l}$, $S^{II}_{j,k,l}$, $S^{III}_{j,k,l}$ and $S^{IV}_{j,k,l}$, respectively. The detailed 3D sub-grid connectivity is given by

$$\begin{aligned}
&S^u_{j,k,l} = (\boldsymbol{\xi}_{j,k,l}, \boldsymbol{\xi}_{j+1,k,l}, \boldsymbol{\xi}_{j,k+1,l}, \boldsymbol{\xi}_{j,k,l+1}), \qquad S^d_{j,k,l} = (\boldsymbol{\xi}_{j+1,k,l+1}, \boldsymbol{\xi}_{j+1,k+1,l+1}, \boldsymbol{\xi}_{j+1,k+1,l}, \boldsymbol{\xi}_{j,k+1,l+1}),\\
&S^I_{j,k,l} = (\boldsymbol{\xi}_{j+1,k,l}, \boldsymbol{\xi}_{j+1,k+1,l}, \boldsymbol{\xi}_{j,k+1,l}, \boldsymbol{\xi}_{j,k+1,l+1}), \qquad S^{II}_{j,k,l} = (\boldsymbol{\xi}_{j+1,k,l}, \boldsymbol{\xi}_{j+1,k,l+1}, \boldsymbol{\xi}_{j,k+1,l+1}, \boldsymbol{\xi}_{j,k,l+1}),\\
&S^{III}_{j,k,l} = (\boldsymbol{\xi}_{j,k+1,l}, \boldsymbol{\xi}_{j,k+1,l+1}, \boldsymbol{\xi}_{j,k,l+1}, \boldsymbol{\xi}_{j+1,k,l}), \qquad S^{IV}_{j,k,l} = (\boldsymbol{\xi}_{j+1,k,l}, \boldsymbol{\xi}_{j+1,k+1,l}, \boldsymbol{\xi}_{j,k+1,l+1}, \boldsymbol{\xi}_{j+1,k,l+1}).
\end{aligned} \tag{16}$$

In the following, we will replace the multi-index (k,l) and (j,k,l) again by one mono-index j, hence writing $S_{i,j}$, where i refers again to the element T_i on the main grid and j to the corresponding element number on the sub-grid. Note that the sub-grid connectivity is the *same* for each element T_i, since all sub-elements are defined on the reference element T_e and are then simply mapped to physical coordinates via the linear mapping (5).

For alternative sub-cell divisions on simplex meshes, see [80,103] and the work by Wang et al. on spectral finite volume schemes [138,139,96]. However, the divisions proposed in [80,103,139,96] are rather complex and difficult to code in an automatic way for very high orders of accuracy, compared to the very simple set of formulae (14), (15) and (16) used here.

An *alternative data representation* $\mathbf{v}_h(\mathbf{x}, t^n)$ on the sub-cells is now expressed by a set of piecewise constant sub-cell averages $v^n_{i,j}$. Those are computed as the L_2 projection of $\mathbf{u}_h$ onto the space of piecewise constant functions on $S_{i,j}$, i.e. they are the simple cell average of $\mathbf{u}_h$ on $S_{i,j}$ given by:

$$\mathbf{v}^n_{i,j} = \frac{1}{|S_{i,j}|} \int_{S_{i,j}} \mathbf{u}_h(\mathbf{x}, t^n) d\mathbf{x} = \frac{1}{|S_{i,j}|} \int_{S_{i,j}} \phi_l(\mathbf{x}) d\mathbf{x}\, \hat{\mathbf{u}}^n_l, \qquad \forall S_{i,j} \in \mathcal{S}_i\,, \tag{17}$$

where we denote by $\mathcal{S}_i = \bigcup_j S_{i,j}$ the set of all sub-cells inside T_i. The projection operator (17) above is in the following also abbreviated by $\mathbf{v}^n_h = \mathcal{P}\left(\mathbf{u}^n_h\right)$.

3.1.2. Sub-cell finite volume update

Using the new data representation $\mathbf{v}_h(\mathbf{x}, t^n)$ (i.e. piecewise constant data $\mathbf{v}^n_{i,j}$ on sub-cells) as initial conditions, the discrete solution at time t^{n+1}, $\mathbf{v}_h(\mathbf{x}, t^{n+1})$, is re-computed by means of a robust one-step finite volume scheme on the

sub-grid. Any scheme from the finite volume family can be considered as long as it is sufficiently robust for the PDE system under consideration; 1st order FV, 2nd order TVD, 3rd/5th order WENO, etc. In this paper we adopt a second order ADER finite volume scheme [55], based on a second order TVD reconstruction that uses the standard Barth & Jespersen [19] slope limiter on unstructured meshes. For the second order scheme, the necessary time evolution based on the Cauchy–Kovalewski procedure is trivial. As a particular feature of our sub-grid finite volume scheme, we apply the Barth & Jespersen limiter also to the slope in *time direction*, i.e. to the time derivative that results from the Cauchy–Kovalewski procedure. However, it is also possible to use a very simple first order Godunov-type scheme. This is the crudest choice, but it is a very cheap and still viable option, as long as the number of sub-cells is sufficiently large. Some numerical results will assess this statement. In the following, we will denote the update of $\mathbf{v}_h$ via the second order ADER TVD finite volume scheme on the subgrid simply by

$$\mathbf{v}_h^{n+1} = \mathcal{A}\left(\mathbf{v}_h^n\right). \tag{18}$$

The initial condition and the boundary conditions needed by the operator $\mathcal{A}\left(\mathbf{v}_h^n\right)$ on the boundaries ∂T_i of element T_i are provided similar to [62] in the following way:

$$\mathbf{v}_h^n(\mathbf{x}, t^n) = \begin{cases} \mathcal{P}\left(\mathbf{u}_h(\mathbf{x}, t^n)\right) & \text{if} \quad \beta_k^n = 0, \\ \mathcal{A}\left(\mathbf{v}_h(\mathbf{x}, t^{n-1})\right) & \text{if} \quad \beta_k^n = 1, \end{cases} \qquad \mathbf{x} \in T_k, \qquad \forall T_k \in \mathcal{N}_i, \tag{19}$$

where $\mathcal{N}_i$ denotes only the direct Neumann neighborhood of element T_i, i.e. all elements which share a common edge (2D) or face (3D) with element T_i. The troubled zones indicator β_k^n indicates an unlimited cell for $\beta_k^n = 0$ and a troubled cell for $\beta_k^n = 1$. More details on the computation of β_k^n are given below in Section 3.2. Relation (19) states that if a cell T_k was unlimited at time t^n, the sub-grid data are computed by the projection operator $\mathcal{P}$ applied to the DG polynomial $\mathbf{u}_h$, whereas for a troubled cell the sub-cell finite volume averages that have been computed inside T_i by the operator $\mathcal{A}\left(\mathbf{v}_h(\mathbf{x}, t^{n-1})\right)$ and which have been subsequently stored there, are directly taken as initial and boundary conditions for the operator $\mathcal{A}\left(\mathbf{v}_h(\mathbf{x}, t^n)\right)$. We emphasize that the alternative solution representation $\mathbf{v}_h^n$ needs to be stored *only* in troubled cells, i.e. in cells T_i with $\beta_i^n = 1$. For unlimited cells, $\mathbf{v}_h^n$ can be computed at any time on demand by the projection operator $\mathcal{P}$. Note that in the Cartesian case [62], a third order ADER-WENO finite volume scheme was used on the subgrid and hence required the entire Voronoi neighborhood $\mathcal{V}_i$ of element T_i, i.e. it involved all neighboring elements that have a common vertex with T_i. In contrast, the second order ADER TVD finite volume scheme used at the subcell level only requires the direct edge/face neighbors of T_i. This makes our limiter *compact* on the main grid and thus fits very well into the philosophy of DG schemes that work on the minimal stencil $\mathcal{N}_i$. This is particularly true thanks to the use of fully-discrete one-step ADER-DG schemes on the main grid and ADER finite volume schemes on the subgrid, since they carry out one entire high order time step on the minimal stencil $\mathcal{N}_i$, while Runge–Kutta time discretizations have a larger effective stencil per time step due to the necessary intermediate Runge–Kutta stages. We stress that in the ADER framework, also the limiter itself is only applied once per time step, and not in each Runge–Kutta stage again. Similar observations have been already made by Qiu et al. in [112].

To obtain a conservative scheme, we emphasize that also the neighbors of troubled cells need to be updated, taking into account the new fluxes that arise across element interfaces due to the finite volume scheme used in the troubled cells.

3.1.3. From sub-cells to cells

Once a robust sub-cell solution $\mathbf{v}_h(\mathbf{x}, t^{n+1})$ has been recomputed for a troubled cell T_i, the piecewise polynomial solution of the DG scheme on the main grid must be recovered. This is achieved by requiring that the sub-cell solution $\mathbf{v}_{i,j}^{n+1}$ in $S_{i,j}$ be equal to the L_2 projection of the unknown DG polynomial $\mathbf{u}_h(\mathbf{x}, t^{n+1})$ onto $S_{i,j}$

$$\int_{S_{i,j}} \mathbf{u}_h(\mathbf{x}, t^{n+1})\, d\mathbf{x} = \int_{S_{i,j}} \mathbf{v}_h(\mathbf{x}, t^{n+1})\, d\mathbf{x}, \qquad \forall S_{i,j} \in \mathcal{S}_i\,. \tag{20}$$

The previous equation is equivalent to solving

$$\frac{1}{|S_{i,j}|} \int_{S_{i,j}} \phi_l(\mathbf{x}) d\mathbf{x}\, \hat{\mathbf{u}}_l^{n+1} = \mathbf{v}_{i,j}^{n+1}, \qquad \forall S_{i,j} \in \mathcal{S}_i\,, \tag{21}$$

which is a standard reconstruction problem arising in the finite volume context. Since we use $N_s = 2N + 1$ the resulting system (21) is *overdetermined*, and is solved via a constrained least-squares reconstruction operator [54], with the linear constraint

$$\int_{T_i} \mathbf{u}_h(\mathbf{x}, t^n)\, d\mathbf{x} = \int_{T_i} \mathbf{v}_h(\mathbf{x}, t^n)\, d\mathbf{x} \tag{22}$$

that requires the reconstruction to be *conservative* on cell T_i. The reconstruction operator (20) and (22) is in the following abbreviated by $\mathbf{u}_h^{n+1} = \mathcal{R}(\mathbf{v}_h^{n+1})$. It can be seen easily that by construction the reconstruction operator and the projection

operator fulfill the condition $\mathcal{R} \circ \mathcal{P} = \mathcal{I}$, where $\mathcal{I}$ is the identity operator. With these operators, the DG limiter for $\mathbf{u}_h^{n+1}$ in troubled cells formally reads

$$\mathbf{u}_h^{n+1} = \mathcal{R}\left(\mathcal{A}(\mathbf{v}_h^n)\right), \tag{23}$$

with $\mathbf{v}_h^n$ given by (19).

This section has described in detail the projection $\mathcal{P}$ and the reconstruction $\mathcal{R}$ operator, as well as the sub-cell based finite volume update $\mathcal{A}$ of troubled DG cells. It remains to detect those troubles cells, i.e. we need to define the troubled zones indicator β_i^n.

3.2. Detection criteria

The appearance of possible spurious oscillations due to the effect of Gibbs phenomenon renders the candidate DG solution not acceptable everywhere in the computational domain. Some cells may demand more numerical dissipation. Our sub-cell limiting strategy, like any limiting strategy, must design a mechanism to detect troubled/problematic/bad cells. In this work we construct a number of detection criteria which are devoted to promote the candidate DG solution in good cells to 'acceptable', and, more important, to list the troubled cells. As already mentioned in the Multi-dimensional Optimal Order Detection (MOOD) paradigm [28,40,41,100], the detection of troubled cells is based on physical considerations and it mostly consists of checking if $\mathbf{u}_h^*(\mathbf{x}, t^{n+1})$ verifies some physical admissibility constraints for the cell T_i. Those are dictated by the system of PDEs resolved and are denoted as the *Physical Admissibility Detection* criteria (PAD). For the hydrodynamics equations these constraints are mainly related to the positivity of density and pressure, whereas, for instance, in a relativistic magneto-hydrodynamics context the boundedness of the velocity by the speed of light is also mandatory [100]. Furthermore, the candidate solution $\mathbf{u}_h^*(\mathbf{x}, t^{n+1})$ is explicitly checked for the occurrence of *floating point errors*, i.e. not-a-number (`NaN`) values that may have been produced by unphysical divisions by zero or by taking roots of negative numbers. In FORTRAN, this is conveniently done with the `ISNAN` command. As a result, floating point errors are not only immediately *found* by the present *a posteriori* detection procedure, but thanks to the *a posteriori* limiting framework, they can even be subsequently *cured* in the more robust sub-cell finite volume scheme. Its ability to cure floating point errors *a posteriori* is a *unique* feature of our DG limiter that distinguishes it from all other existing DG limiters. It is made possible because the sub-cell finite volume scheme will start again from physically admissible data that were saved at the *previous time level* t^n. This very particular feature can also be seen as an element-by-element *checkpointing* and *restarting* of the solver. It is obvious that this significantly enhances the robustness and fault tolerance of the high order DG scheme proposed in this paper.

The second set of detection criteria deals with numerical issues, such as spurious oscillations, and is referred to as *Numerical Admissibility Detection* criteria (NAD). NAD rely on relaxed *discrete maximum principle* (DMP) in the sense of polynomials $\mathbf{u}_h(\mathbf{x}, t^n)$ as

$$\min_{\mathbf{y}\in\mathcal{V}_i}\left(\mathbf{u}_h(\mathbf{y}, t^n)\right) - \delta \;\le\; \mathbf{u}_h^*(\mathbf{x}, t^{n+1}) \;\le\; \max_{\mathbf{y}\in\mathcal{V}_i}\left(\mathbf{u}_h(\mathbf{y}, t^n)\right) + \delta \qquad \forall \mathbf{x} \in T_i\,, \tag{24}$$

where the set $\mathcal{V}_i$ contains the current cell T_i and its Voronoi neighborhood $\mathcal{V}_i$, i.e. the cells that share at least a common node with T_i. The use of a DMP in the sense of polynomials has been inspired by the work on positivity preserving schemes of Zhang and Shu, see [144,145,79]. Eqn. (24) expresses the fact that the polynomial representing the candidate solution $\mathbf{u}_h^*(., t^{n+1})$ in cell T_i must remain between the minimum and the maximum values of the polynomials representing the solution at the previous time step $\mathbf{u}_h(., t^n)$ in the set $\mathcal{V}_i$. The small number δ in (24) is a parameter used to relax the discrete maximum principle thus allowing for very small undershoots and overshoots, which permits to maintain a good accuracy when dealing with smooth extrema. The value used in [62] and adopted in this work is

$$\delta = \max\left(\epsilon_0, \epsilon\left(\max_{\mathbf{y}\in\mathcal{V}_i}\left(\mathbf{u}_h(\mathbf{y}, t^n)\right) - \min_{\mathbf{y}\in\mathcal{V}_i}\left(\mathbf{u}_h(\mathbf{y}, t^n)\right)\right)\right), \tag{25}$$

where we usually set $\epsilon = 10^{-3}$ and $\epsilon_0 = 10^{-4}$. In other words, parameter δ defined by (25) allows the occurrence of new extrema the values of which do not exceed one thousandth of the local jump present at t^n in the neighborhood of the current cell. The value ϵ_0 is needed in the case where the jump is zero.

From a practical point of view dealing with (24), that is, inequalities defined on possibly high order polynomials, is complex. Instead we use the alternative data representations (17) $\mathbf{v}_h(\mathbf{x}, t^n)$ and $\mathbf{v}_h^*(\mathbf{x}, t^{n+1})$ on the sub-cells respectively corresponding to initial data $\mathbf{u}_h^n$ and candidate solution $\mathbf{u}_h^*$. Consequently (24) becomes for a given cell index i

$$\min_{k\in\mathcal{V}_i,\, l\in\mathcal{S}_k} \mathbf{v}_{k,l}^n - \delta \;\le\; \mathbf{v}_{i,j}^{*,n+1} \;\le\; \max_{k\in\mathcal{V}_i,\, l\in\mathcal{S}_k} \mathbf{v}_{k,l}^n + \delta\,, \quad \forall\, j \in \mathcal{S}_i. \tag{26}$$

Analogous to (26), also the *point values* of the discrete solution on the sub grid are tested against the DMP. In practice, if a cell does not fulfill the PAD criteria, then it is flagged as problematic and must be recomputed. Next the NAD criteria are tested for the remaining cells which may or may not be flagged as problematic. The result of this step is a list of problematic cells along with a patch of surrounding neighbor cells; these form the so-called troubled cells which are re-computed with

the sub-cell FV scheme described previously. In our approach each conserved variable is tested for the DMP, but also other variables like the primitive variables or the entropy could be tested for the satisfaction of the DMP.

In this approach, physical and the numerical criteria are totally independent. Consequently the relaxation of the maximum principle never affects the positivity of the solution. More important, the detection is performed at time level t^{n+1}, but using the extrema at the old time level t^n, whereas classical indicators typically use information from only one time level, generally either t^n or t^{n+1}. This subtle but crucial difference allows for a 'simple' *observation* of problems which have occurred during the timestep, contrarily to classical finite volume limiting strategies that use data at time t^n, and which must solve the more difficult problem of *predicting* their occurrence.

4. Numerical results

For most test cases presented in this section we have employed the ADER Discontinuous Galerkin method (10) with piecewise approximation polynomials of degree $N = 4$ or $N = 5$, referred to as ADER-DG-$\mathbb{P}_N$ in the following. This unlimited DG scheme is then supplemented with the new *a posteriori* sub-cell limiter (SCL) on unstructured simplex meshes proposed in this paper. If not stated otherwise, the scheme acting at the sub-cell level is always a second order TVD finite volume scheme with Barth and Jespersen [19] slope limiter. In one case, we also use a simple first order Godunov-type scheme, in order to assess its performance against the more sophisticated second order TVD scheme on the sub-grid level. By default the numerical flux function and the path-conservative jump term used in most of the simulations is the simple Rusanov scheme (11).

Since each variable inside a computational cell is represented by a polynomial of degree $N > 0$, we plot the numerical solution $\mathbf{u}_h(\mathbf{x}, t^n)$ as point values evaluated on a sub-grid made of $N_p = N + 1$ sub-points per edge, if the cell is unlimited.[3] The topology of the visualization subgrid is the same as the one used for the subcell limiter, depicted in Figs. 1 and 2, but with less sampling points. For troubled cells, we plot the alternative representation of the solution $\mathbf{v}_h(\mathbf{x}, t^n)$ on the sub-grid used for the limiter with $N_s = 2N + 1$. For a more sophisticated alternative visualization technique of piecewise polynomial data see [21].

We systematically represent the cells detected as troubled in red, while valid cells are colored in blue when the limiter is shown.

For 1D cuts we usually take equidistant samples at sub-grid level of the solution representations $\mathbf{u}_h(\mathbf{x}, t^n)$ and $\mathbf{v}_h(\mathbf{x}, t^n)$, respectively. This is important to verify that the subscale structure of the DG polynomials really represents a physically valid state within one large cell. As such a limiter for the DG method should be able to maintain smooth solutions, and, more importantly, keep the ability of the DG scheme to reproduce discontinuous profiles at shock waves and steep fronts without spurious oscillations. This must hold for the entire discrete solution $\mathbf{u}_h(\mathbf{x}, t^n)$, and not only for its mean values on the main grid.

4.1. Euler equations of compressible gas dynamics

In this section we solve the Euler equations of compressible gas dynamics

$$\frac{\partial}{\partial t}\begin{pmatrix}\rho\\ \rho\mathbf{v}\\ \rho E\end{pmatrix} + \nabla\cdot\begin{pmatrix}\rho\mathbf{v}\\ \rho\mathbf{v}\otimes\mathbf{v} + p\,\mathbf{I}\\ \mathbf{v}(\rho E + p)\end{pmatrix} = 0, \tag{27}$$

with the ideal gas EOS

$$p = (\gamma - 1)\left(\rho E - \frac{1}{2}\rho\mathbf{v}^2\right). \tag{28}$$

Here, ρ denotes the fluid density, $\mathbf{v} = (u, v, w)$ is the velocity vector, p is the fluid pressure, $\mathbf{I}$ denotes the identity matrix and ρE is the total energy density. The PAD criteria, which depend on the underlying physics, that is the system of PDEs solved, are the positivity of density and pressure for the Euler equations.

4.1.1. Isentropic vortex in motion

The isentropic vortex problem was introduced in [7,78] to test the accuracy of numerical methods, since the exact solution is smooth and has an analytical expression. The computational domain is the square $\Omega = [0; L] \times [0; L]$ of length $L = 10$. The ambient base flow far from the vortex is characterized by $\rho_\infty = 1.0$, $u_\infty = 1.0$, $v_\infty = 1.0$, $w_\infty = 0.0$, $p_\infty = 1.0$, with a normalized ambient temperature $T^*_\infty = 1.0$. A ratio of specific heats of $\gamma = 1.4$ is considered. A vortex is centered at $(x_{\text{vortex}}, y_{\text{vortex}}) = (5, 5)$ and is added as a perturbation to the ambient gas at the initial time $t = 0$ with $u = u_\infty + \delta u$, $v = v_\infty + \delta v$, $w = w_\infty$, $T^* = T^*_\infty + \delta T^*$ where

[3] Note that for a DG-$\mathbb{P}_5$ scheme the number of degrees of freedom per cell is 56 in 3D, 21 in 2D, and 6 in 1D. The size of the sub-grid used for the visualization of $\mathbf{u}_h(\mathbf{x}, t^n)$ in unlimited cells must therefore also adapt to these numbers.

Table 1
L^1, L^2 and L^∞ errors and convergence rates for the 2D isentropic vortex problem for the ADER-DG-$\mathbb{P}_N$ scheme with sub-cell limiter for variable ρ at a final time of $t = 10$.

2D isentropic vortex problem – ADER-DG-$\mathbb{P}_N$ + FV SCL									
	N_x	L^1 error	L^2 error	L^∞ error	L^1 order	L^2 order	L^∞ order	Theor.	d.o.f.
DG-$\mathbb{P}_2$	24	2.3877E–01	6.4365E–02	4.7932E–02	–	–	–	3	7788
	32	1.2517E–02	2.8209E–02	2.6350E–02	2.24	2.87	2.08		13752
	64	1.1262E–02	1.6989E–03	2.2497E–03	3.47	4.05	3.55		55152
	128	3.6726E–04	8.1964E–05	2.2295E–04	4.94	4.37	3.33		221568
DG-$\mathbb{P}_3$	24	6.9065E–03	9.9366E–04	1.1301E–03	–	–	–	4	12980
	32	2.1032E–03	3.0299E–04	3.0041E–04	4.13	4.13	4.61		22920
	64	4.4259E–04	6.7345E–05	6.9601E–05	3.84	3.71	3.61		91920
	128	1.5027E–04	2.5743E–05	2.9970E–05	3.81	3.56	3.33		369280
DG-$\mathbb{P}_4$	24	1.0320E–03	1.4885E–04	1.8733E–04	–	–	–	5	19470
	32	2.7838E–04	3.9632E–05	3.8471E–05	4.55	4.60	5.50		34380
	64	4.1103E–05	6.2085E–06	1.0498E–05	4.72	4.57	3.20		137880
	128	1.0079E–05	1.5731E–06	2.2113E–06	4.79	4.65	4.12		553920
DG-$\mathbb{P}_5$	12	8.6717E–03	1.2917E–03	1.7776E–03	–	–	–	6	6720
	16	1.4106E–03	2.0843E–04	2.3721E–04	6.31	6.34	7.00		12180
	24	1.3297E–04	1.9177E–05	2.3855E–05	5.82	5.88	5.66		27258
	32	2.2986E–05	3.1365E–06	3.7173E–06	6.10	6.29	6.46		48132
DG-$\mathbb{P}_6$	8	1.8686E–01	3.3608E–02	2.9686E–02	–	–	–	7	4200
	12	7.2299E–03	1.0920E–03	1.1755E–03	8.02	8.45	7.96		8960
	16	3.6699E–04	5.4813E–05	7.3540E–05	10.36	10.40	9.63		16240
	24	2.0292E–05	2.9712E–06	4.4511E–06	7.14	7.19	6.92		36344

$$\delta u = -y' \frac{\beta}{2\pi} \exp\left(\frac{1-r^2}{2}\right), \quad \delta v = x' \frac{\beta}{2\pi} \exp\left(\frac{1-r^2}{2}\right), \quad \delta T^* = -\frac{(\gamma-1)\beta}{8\gamma\pi^2} \exp\left(1-r^2\right),$$

with $r = \sqrt{x'^2 + y'^2}$ and $x' = x - x_{\text{vortex}}$, $y' = y - y_{\text{vortex}}$. The vortex strength is $\beta = 5.0$ and the initial density is defined by

$$\rho = \rho_\infty \left(\frac{T^*}{T^*_\infty}\right)^{\frac{1}{\gamma-1}} = \left(1 - \frac{(\gamma-1)\beta}{8\gamma\pi^2} \exp\left(1-r^2\right)\right)^{\frac{1}{\gamma-1}}. \tag{29}$$

Periodic boundary conditions are prescribed everywhere, so that at the final time $t_{\text{final}} = 10$ the vortex is back to its original position.

This problem has a smooth solution and thus must be solved with effective high-order of accuracy by any high order scheme. Consequently, we compute the discrete L^1, L^2 and L^∞ error norms between the exact solution and the numerical solution $\mathbf{u}_h$ for the density variable on a sequence of successively refined triangular grids. This allows us to compute the effective numerical order of accuracy of the schemes which are tested. The unstructured meshes are constructed so that the edge length of the triangles on the boundary of Ω is $h = L/N_x$, starting from $N_x = 8$ (coarse grid) up to $N_x = 128$ (fine grid). In Table 1 we report the obtained error norms and the corresponding rates of convergence for ADER-DG-$\mathbb{P}_N$ schemes with N varying from 2 to 6. We would like to emphasize that the *a posteriori* sub-cell limiter is active for all schemes, but, as expected, the PAD and NAD criteria are either not detecting any troubled cells, or only extremely few, as the underlying fluid flow is smooth and if the mesh is fine enough. Consequently the DG schemes are essentially run in their unlimited form and the presence of the *a posteriori* sub-cell limiter does not destroy the formal order of convergence of the underlying DG scheme if the order is high enough and if the mesh is sufficiently refined. To quantify this statement, we run the sixth order ADER-DG-$\mathbb{P}_5$ scheme three times: once with the limiter completely switched off, once with the limiter active according to the PAD and NAD criteria specified above, and once with the limiter switched on artificially for all cells. The resulting convergence rates are shown in Table 2. One can observe that the error norms with active limiter and without limiter are exactly the same, while the convergence rate clearly reduces to between first and second order of accuracy in the case if the limiter is activated for all cells, as expected.

4.1.2. Steady 2D flow around a circular cylinder

In this section, we simulate the steady flow over a circular cylinder. This test case has been used, for example, by Bassi & Rebay [20] and by Krivodonova & Berger [93] in order to assess the performance of high order discontinuous Galerkin finite element schemes in the presence of curved solid wall boundaries. The computational domain of our setup is the square $\Omega = [-5, 5]^2$, in the center of which there is a circular cylinder of radius $R = 1$. The exact solution for the radial and tangential velocity components v_r and v_ϕ as well as the pressure field p of the underlying potential flow problem (which is valid only in the limit $M_\infty \to 0$), is given in polar coordinates (r, ϕ) by:

Table 2
L^1, L^2 and L^∞ errors and convergence rates for the 2D isentropic vortex problem for the ADER-DG-$\mathbb{P}_5$ scheme with sub-cell limiter switched off, with *a posteriori* subcell limiter as described in this paper, and with limiter artificially activated for all cells. Error norms are shown for variable ρ at final time 10.

2D isentropic vortex problem – ADER-DG-$\mathbb{P}_5$						
N_x	L^1 error	L^2 error	L^∞ error	L^1 order	L^2 order	L^∞ order
ADER-DG-$\mathbb{P}_5$ (unlimited)						
12	8.6717E–03	1.2917E–03	1.7776E–03	–	–	–
16	1.4106E–03	2.0843E–04	2.3721E–04	6.31	6.34	7.00
24	1.3297E–04	1.9177E–05	2.3855E–05	5.82	5.88	5.66
32	2.2986E–05	3.1365E–06	3.7173E–06	6.10	6.29	6.46
ADER-DG-$\mathbb{P}_5$ (*a posteriori* subcell limiter)						
12	8.6717E–03	1.2917E–03	1.7776E–03	–	–	–
16	1.4106E–03	2.0843E–04	2.3721E–04	6.31	6.34	7.00
24	1.3297E–04	1.9177E–05	2.3855E–05	5.82	5.88	5.66
32	2.2986E–05	3.1365E–06	3.7173E–06	6.10	6.29	6.46
ADER-DG-$\mathbb{P}_5$ (all cells limited)						
12	3.7013E–02	8.3822E–03	6.6955E–03			
16	2.3559E–02	5.5033E–03	4.6471E–03	1.57	1.46	1.27
24	1.4280E–02	3.3287E–03	2.7832E–03	1.23	1.24	1.26
32	1.0185E–02	2.3863E–03	1.7884E–03	1.17	1.16	1.54

Table 3
L_2 norms of the relative entropy errors and associated convergence rates with respect to the coarsest grid for the 2D flow over a circular cylinder at time $t = 100$ for ADER-DG-$\mathbb{P}_2$ and ADER-DG-$\mathbb{P}_4$ schemes.

ADER-DG-$\mathbb{P}_2$	$h = 1$	$h = 1/2$	$h = 1/4$	$h = 1/10$
L_2 norm	1.4807E–01	2.4506E–03	4.9689E–04	3.7077E–05
L_2 order		5.92	4.11	3.60
ADER-DG-$\mathbb{P}_4$	$h = 3/4$	$h = 1/2$	$h = 1/3$	$h = 1/4$
L_2 norm	6.9919E–02	2.5057E–04	8.5796E–05	4.4128E–05
L_2 order		13.89	8.27	6.71

$$v_r(r,\phi) = M_\infty \sqrt{\frac{\gamma p_\infty}{\rho_\infty}} \left(1 - \frac{R^2}{r^2}\right) \cos\phi, \qquad v_\phi(r,\phi) = -M_\infty \sqrt{\frac{\gamma p_\infty}{\rho_\infty}} \left(1 + \frac{R^2}{r^2}\right) \sin\phi, \tag{30}$$

$$p\,(r,\theta) = p_\infty \left(1 + \frac{1}{2}\gamma M_\infty^2\right) - \frac{1}{2}\rho_\infty \left(v_r^2 + v_\theta^2\right). \tag{31}$$

For our test case, we use a free stream Mach number of $M_\infty = 0.38$, as suggested in [20,93], a free stream density and pressure of $\rho_\infty = \gamma$ and $p_\infty = 1$, respectively, and the ratio of specific heats is chosen as $\gamma = 1.4$. The incoming flow is parallel to the x-axis. In this subsonic flow regime the potential flow is still a reasonable approximation of the flow field and for isentropic compressible flows, the density can be computed as

$$\rho = \rho_\infty \left(\frac{p}{p_\infty}\right)^{1/\gamma}. \tag{32}$$

In our simulations, we use the exact solution above as initial and boundary conditions and use an ADER-DG-$\mathbb{P}_2$ scheme on a sequence of successively refined meshes of characteristic size $h = 1$, $h = 1/2$, $h = 1/4$ and $h = 1/10$, respectively. Furthermore, the same test is run with an ADER-DG-$\mathbb{P}_4$ method on a sequence of meshes with size $h = 3/4$, $h = 1/2$, $h = 1/3$ and $h = 1/4$, respectively. For this test we set $\epsilon = \epsilon_0 = 10^{-2}$. In order to discretize the curved boundaries, we use high order *isoparametric* elements, where the geometry is represented by the same polynomial degree as the discrete solution for the PDE, as suggested in [20]. The resulting relative entropy errors

$$\epsilon_S = \frac{p}{p_\infty} \left(\frac{\rho_\infty}{\rho}\right)^\gamma - 1 \tag{33}$$

and the associated convergence rates are reported in Table 3. In Fig. 3 the Mach isocontour lines are shown, together with the streamlines and a sketch of the unstructured mesh around the cylinder. During the entire simulation, no element has been flagged as troubled.

4.1.3. Sod and Lax shock tube

Here, we run the planar Sod and the classical Lax shock tube problems on a 2D and 3D unstructured mesh. These problems are used to assess the ability of the numerical method to capture one-dimensional simple waves on coarse un-

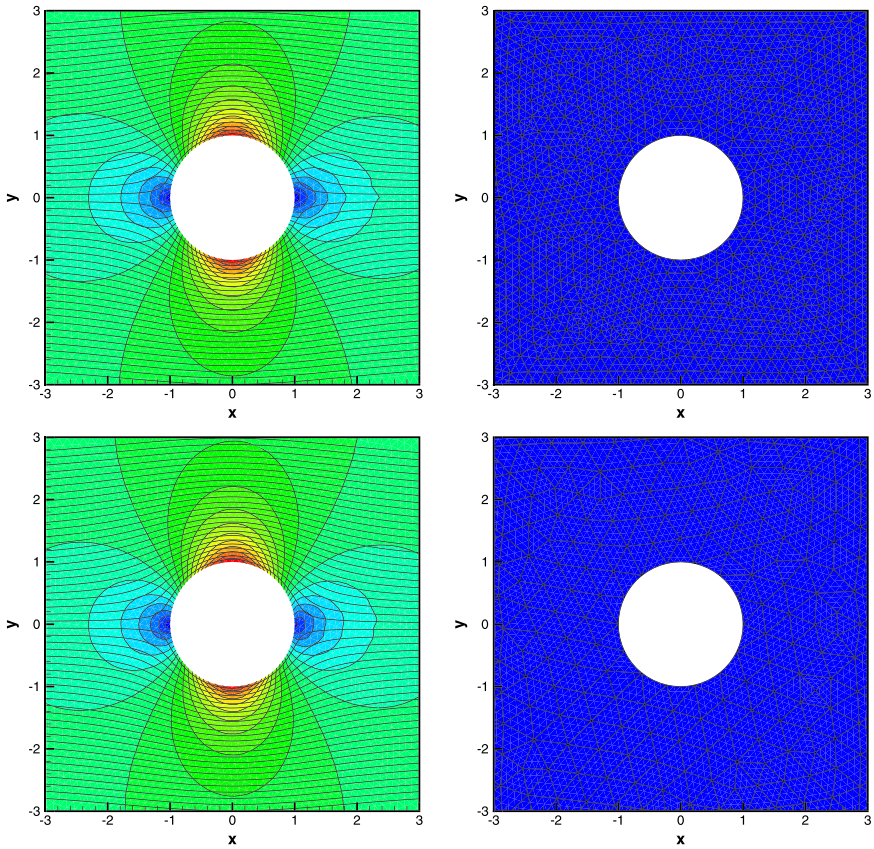

Fig. 3. Steady 2D flow around a circular cylinder with free stream Mach number $M_\infty = 0.38$ at a final time of $t = 100$. Mach isocontours and streamlines (left). A zoom into the unstructured triangular mesh is shown on the right. Unlimited cells are highlighted in blue, while limited cells are completely absent (right). *Isoparametric* ADER-DG-$\mathbb{P}_2$ scheme on a mesh of characteristic size $h = 1/4$ (top) and *isoparametric* ADER-DG-$\mathbb{P}_4$ scheme on a mesh of characteristic size $h = 1/2$ (bottom). Only elements adjacent to the cylinder wall are curved. (For interpretation of the references to color in this figure legend, the reader is referred to the web version of this article.)

Table 4
Initial left and right states for the density ρ, velocity u and the pressure p for the Sod and Lax shock tube problems. Final simulation times t_{final} are also provided.

Problem	Left state			Right state			Final time
	ρ_L	u_L	p_L	ρ_R	u_R	p_R	t_{final}
Sod	1.0	0.0	1.0	0.125	0.0	0.1	0.2
Lax	0.445	0.698	3.528	0.5	0.0	0.571	0.14

structured meshes. Indeed, the size of the main grid cells is not the characteristic length scale on which one wishes to capture the shock wave, but one rather desires to capture the shock on a scale of the order $h/(N+1)$, which corresponds to the effective resolution of a high order DG scheme. The proposed *a posteriori* sub-cell FV limiter spreads such simple waves only over one or two sub-cells, thanks to the use of a high resolution shock capturing TVD scheme at the sub-grid level.

The initial conditions are listed in Table 4. The other velocity components are initialized with 0. The ratio of specific heats is $\gamma = 1.4$ and for both problems the initial discontinuity is located in $x = 0$. The exact solution for these one-dimensional Riemann problems can be found in [133]. For the two-dimensional setup, the computational domain is given by $\Omega = [-0.5; 0.5] \times [-0.05; 0.05]$ and is paved with an unstructured mesh with characteristic mesh size of $h = 1/100$ and composed of 2226 triangles, see Fig. 5. For the three-dimensional setup, the domain is $\Omega = [-0.5; 0.5] \times [-0.05; 0.05]^2$, while the corresponding tetrahedral mesh with characteristic grid size $h = 1/100$ consists of 67711 elements. In the 2D case, an ADER-DG-$\mathbb{P}_5$ scheme has been used, while we use an ADER-DG-$\mathbb{P}_4$ scheme for the 3D case. In all cases, the second order *a posteriori* sub-cell finite volume limiter is employed. Dirichlet boundary conditions are imposed in x-direction, while periodic boundaries are applied in y and z direction, respectively.

In Fig. 4 the density, the x component of the velocity and pressure are presented for the 2D case at the final time for both problems. The 3D results for the Sod shock tube problem are presented in Fig. 6. In all cases we can observe that the numerical results obtained for the shock waves and the contact discontinuities are extremely sharp. In the 3D simulations

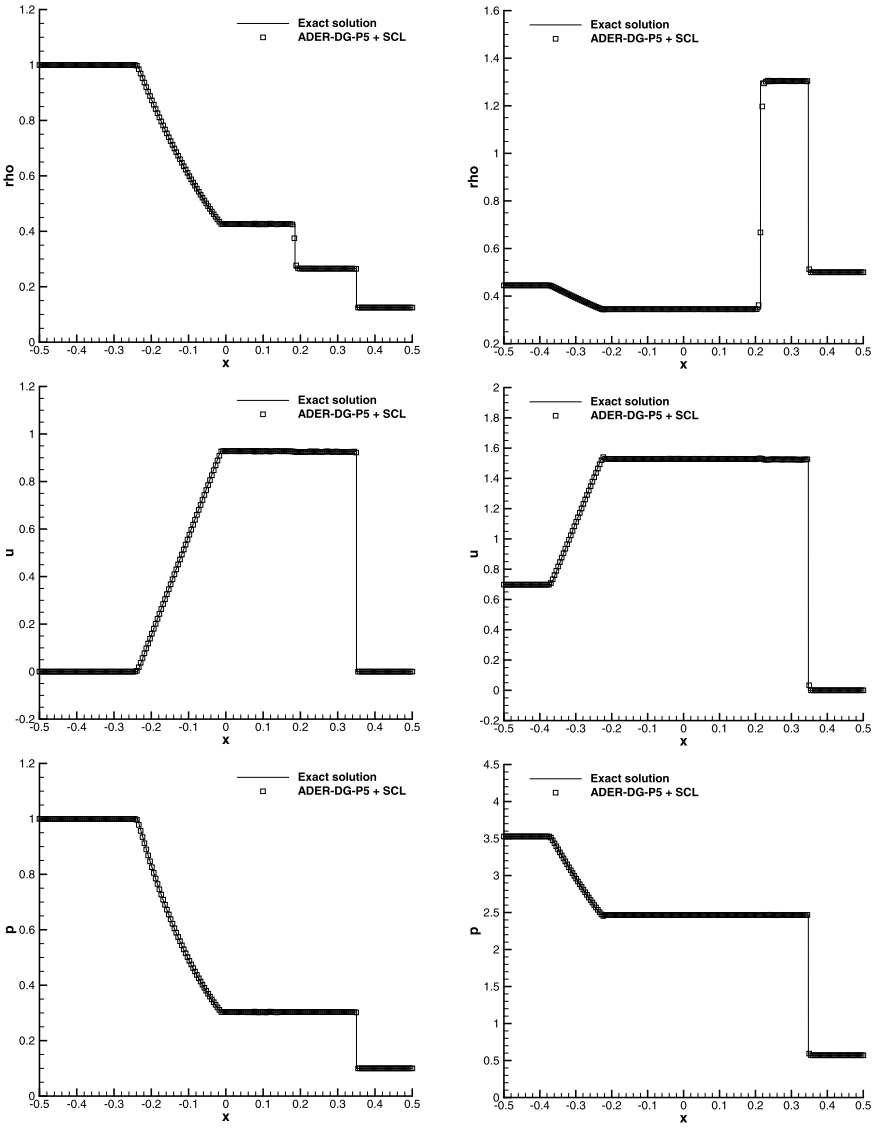

Fig. 4. Sod shock tube problem (left panels) at $t_{\text{final}} = 0.2$ and Lax problem (right panels) at $t_{\text{final}} = 0.14$ solved on a 2D triangular mesh with characteristic mesh spacing $h = 1/100$. An ADER-DG-$\mathbb{P}_5$ scheme supplemented with second order *a posteriori* sub-cell finite volume limiter has been used – 1D cut on 200 equidistant sample points through the numerical solution along the x-axis (symbols) *vs* exact solution for density (top), axial velocity u (middle) and pressure (bottom).

one can observe some spurious oscillations in the velocity, which is a derived quantity and not a conserved variable. In order to reduce these oscillations, one could consider to check the DMP also on the primitive variables.

Also from Figs. 5 and 6 we find that the *a posteriori* limiter is acting at the shock waves, where it is expected, whereas the great majority of the remaining part of the computational domain is essentially simulated with the unlimited high order ADER-DG scheme. Due to the high resolution shock capturing TVD scheme acting as sub-cell limiter, the shock wave is truly captured on a sub-grid scale, and is able to move across a coarse cell on the main grid without generating spurious numerical oscillations. Note that the limiter does not act on the contact wave any more for large times, since the contact discontinuity is a linearly degenerate field, which can be correctly propagated by an unlimited DG scheme once it has been sufficiently smeared by the subcell limiter in the initial phase of the Riemann problem. This is an important feature of our *a posteriori* detector and limiter and has already been observed in [62,143] in the Cartesian grid case.

In order to assess the influence of the choice of the finite volume scheme used on the sub-grid level, in Fig. 5 a direct comparison of the numerical results obtained for the 2D case with a first order and with a second order sub-grid finite volume scheme is shown. At least for these two test problems, the numerical results seem to indicate that the use of a very simple first order finite volume scheme on the sub-grid level is possible and leads only to a rather small increase of the numerical diffusion at shocks and contact discontinuities.

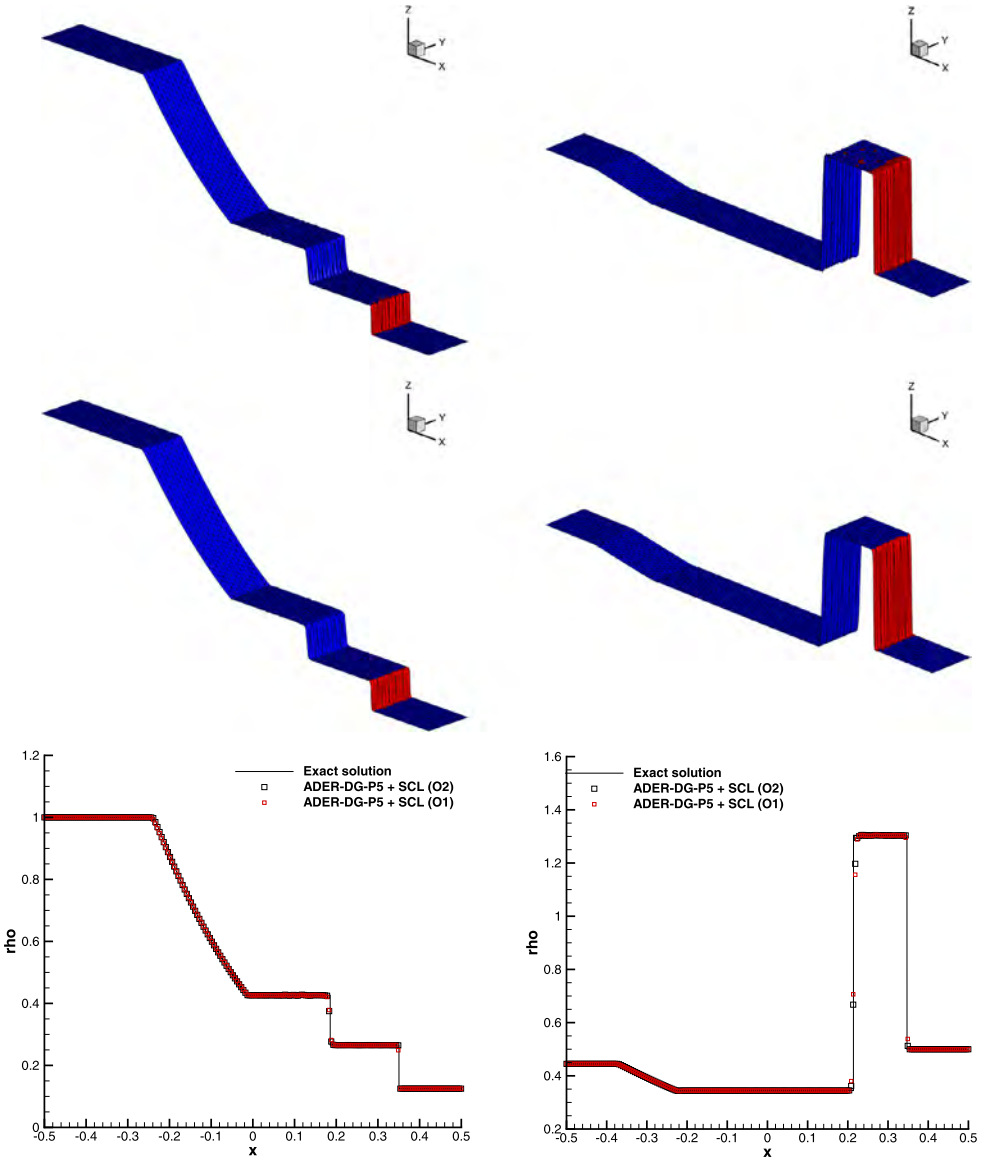

Fig. 5. Sod problem (left column) at $t = 0.2$ and Lax problem (right column) at $t = 0.14$ solved on a triangular mesh with characteristic mesh size $h = 1/100$. An ADER-DG-$\mathbb{P}_5$ scheme with *a posteriori* sub-cell finite volume limiter has been used. Troubled cells are highlighted in red, while unlimited cells are shown in blue. The results in the top row have been obtained with a *second* order TVD scheme on the sub-grid level, while for the results depicted in the middle row, only a *first* order scheme has been employed at the sub-grid level. A direct comparison via a 1D cut along the x-axis is provided in the bottom row. The results indicate that the first order sub-grid FV scheme yields only slightly more diffusive results than those obtained with the second order sub-grid scheme. (For interpretation of the references to color in this figure legend, the reader is referred to the web version of this article.)

4.1.4. Double Mach reflection problem

Let us consider the 2D double Mach reflection problem of a strong shock, first proposed by Woodward and Colella in [140]. This test problem involves a Mach 10 shock in a perfect gas with $\gamma = 1.4$ which hits a ramp at 30° with the x-axis. Using Rankine–Hugoniot conditions we can deduce the pre- and post-shock initial conditions

$$(\rho, u, v, p)(\mathbf{x}, t = 0) = \begin{cases} \frac{1}{\gamma}(8.0, 8.25, 0.0, 116.5), & \text{if} \quad x < 0.0, \\ (1.0, 0.0, 0.0, \frac{1}{\gamma}), & \text{if} \quad x \geq 0.0. \end{cases} \tag{34}$$

Reflecting wall boundary conditions are prescribed on the bottom and on the top of the domain, while the exact solution according to the Rankine–Hugoniot relations is imposed on the left and on the right boundary.

The computational domain is depicted in Fig. 7 and the unstructured mesh is built using a characteristic mesh size of $h = 1/200$, leading to a total of 359016 triangular elements. This problem is solved with an ADER-DG-$\mathbb{P}_4$ scheme, in combination with the *a posteriori* sub-cell finite volume limiter. The computational results are depicted at time $t = 0.2$ in

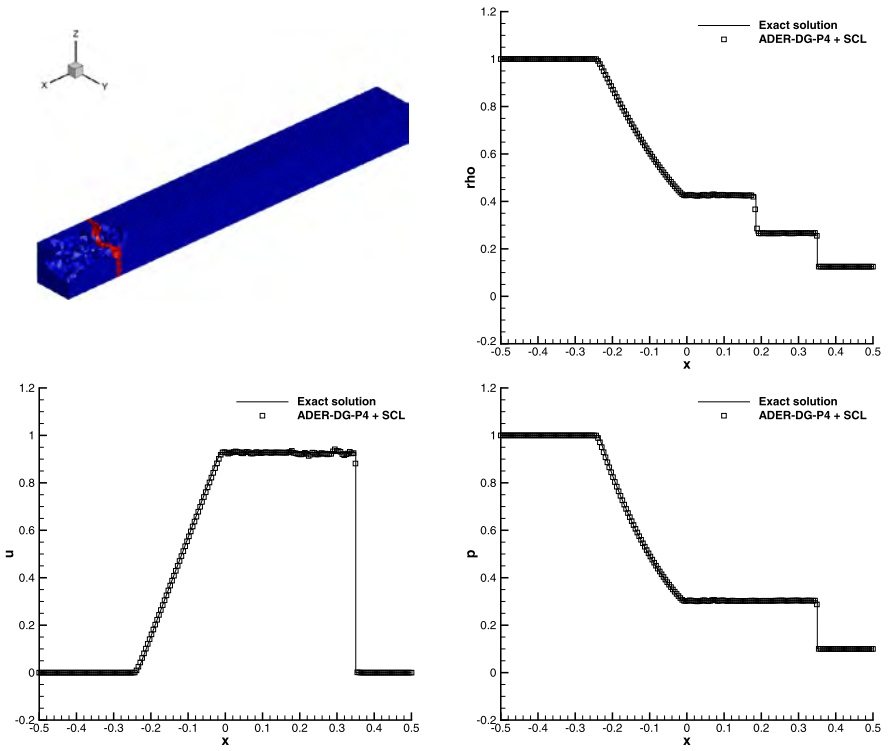

Fig. 6. Sod shock tube problem at $t_{\text{final}} = 0.2$ computed on a 3D tetrahedral mesh with mesh spacing $h = 1/100$. The mesh and the troubled cells highlighted in red are depicted in the top left panel. An ADER-DG-$\mathbb{P}_4$ scheme supplemented with second order *a posteriori* TVD sub-cell finite volume limiter has been used – 1D cut on 200 equidistant sample points through the numerical solution along the x-axis (symbols) *vs* exact solution for density, axial velocity u and pressure. (For interpretation of the references to color in this figure legend, the reader is referred to the web version of this article.)

Fig. 7, where the density contour lines as well as the distribution of the troubled cells are plotted. We observe that the limiter is mostly acting at the shock waves, apart from some spurious activations in the post-shock regions of the incident and the reflected shock wave. To improve this situation, one could consider the recent boxplot outlier approach forwarded by Vuik and Ryan in [137], instead of the simple discrete maximum principle (DMP) used in this paper.

4.1.5. Forward facing step

Next we consider the so called forward facing step (FFS) problem, also proposed by Woodward and Colella in [140]. It is a Mach 3 wind tunnel with a step. The initial condition consists in a uniform gas with density $\rho = \gamma$, pressure $p = 1$, velocity components $u = 3$, $v = 0$ and $\gamma = 1.4$. The computational domain is given by $\Omega = [0; 3] \times [0; 1] \backslash [0.6; 3] \times [0; 0.2]$. Reflective boundary conditions are applied on the upper and lower boundary of the domain, whereas inflow and outflow boundary conditions are applied at the entrance and the exit. The solution of this problem involves shock waves interacting with the wall boundaries. The unstructured mesh consists of 56972 triangular elements of size $h = 1/100$ and the simulation is run up to a final time of $t = 4$. In Fig. 8 we present the results obtained with an ADER-DG-$\mathbb{P}4$ scheme with *a posteriori* second order sub-cell finite volume limiter. For this test problem we can observe that the shock waves are clearly identified, while the shear layer in the upper part of the domain is essentially unlimited and starts to roll up already on this rather coarse mesh.

4.1.6. 2D and 3D explosion problems

Here, we consider a cylindrical as well as a spherical explosion problem in 2D and 3D, respectively. The computational domain is $\Omega = \{\mathbf{x} : \|\mathbf{x}\| \leq R\}$, i.e. the circle (sphere) of radius $R = 1$. In the 3D case, only the half-sphere with $x \geq 0$ and symmetry boundary condition at $x = 0$ is considered, while the 2D simulation considers the entire circle. The computational setup represents a cylindrical/spherical extension of the classical Sod problem [127], with initial conditions given by

$$(\rho, u, v, w, p) = \begin{cases} (1, 0, 0, 0, 1) & \text{for} \quad \|\mathbf{x}\| \leq R_d\,, \\ (0.125, 0, 0, 0, 0.1) & \text{for} \quad \|\mathbf{x}\| > R_d\,, \end{cases} \tag{35}$$

where $R_d = 0.5$ denotes the radius of the initial discontinuity. An ideal-gas equation of state with adiabatic index $\gamma = 1.4$ is considered. The reference solution can be obtained solving an equivalent one dimensional PDE in the radial direction with geometric source terms by using a standard finite volume scheme on a very fine mesh, see [133] for details. An ADER-DG-$\mathbb{P}5$

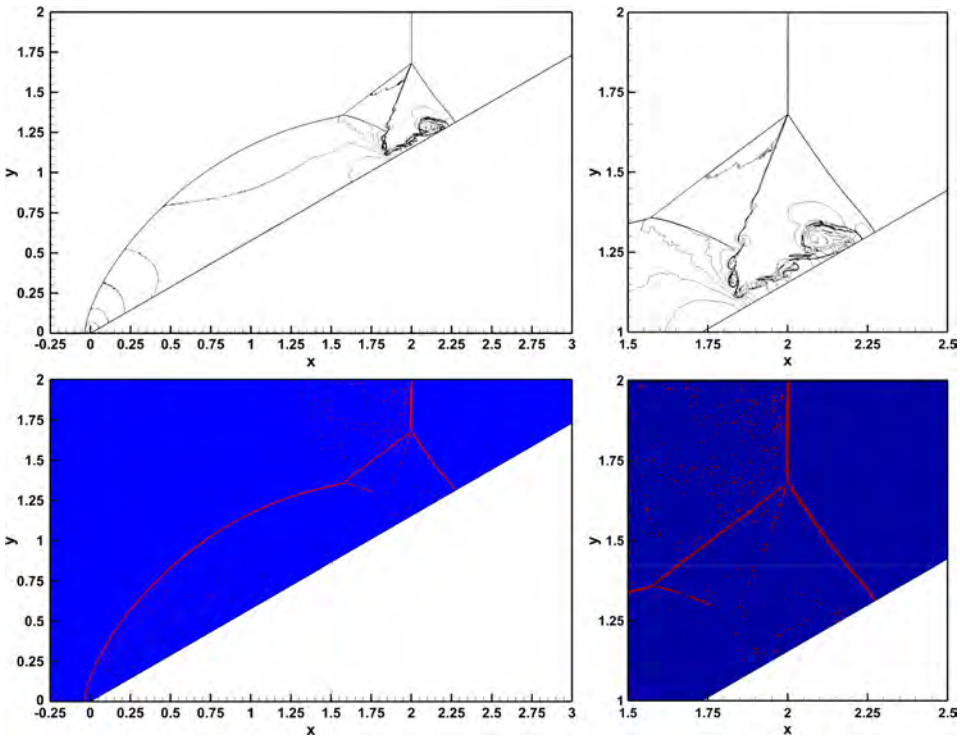

Fig. 7. Double Mach reflection problem obtained with the ADER-DG $\mathbb{P}_4$ scheme and *a posteriori* sub-cell finite volume limiter at time $t = 0.2$ on a grid with mesh spacing $h = 1/200$. Top: equidistant density contour lines from 1.5 to 22.5 (contour spacing $\Delta\rho = 0.5$). Bottom: troubled zones indicator. Left: total view of the numerical solution. Right: zoom around the incident and reflected shocks.

scheme combined with the second order *a posteriori* sub-cell finite volume limiter has been employed. In the 2D case the computational mesh is composed of 68324 triangles with characteristic mesh spacing $h = 1/100$, while the 3D mesh is very coarse and consists only of 877298 tetrahedra with characteristic mesh spacing $h = 1/40$. In the 3D case, this leads to a total number of 17,545,960 spatial degrees of freedom per variable of the PDE system.

Fig. 9 shows the profiles of the density, velocity, pressure and internal energy along the x- axis at time $t = 0.2$, for the two-dimensional case, together with the reference solution. In Fig. 9 we also show a plot of the troubled cells, which are essentially concentrated at the circular shock front, while the intermediate circular contact wave results are unlimited at time $t = 0.2$. Again, this is due to the fact that the contact wave has already undergone some limiting, and hence smearing, during the initial phase of the explosion problem, and can subsequently be transported as a smooth feature by the unlimited ADER-DG scheme, without the production of spurious oscillations. From the zoom depicted on the top right of Fig. 9 one can clearly observe that the shock wave is properly resolved *within* one single element on the main grid. The circular structure of the shock front is furthermore well preserved without noticeable mesh imprinting. The obtained results therefore show that our *a posteriori* sub-cell limiter is able to maintain the sub-cell resolution capabilities of the DG method, while providing robust and non-oscillatory results at shock waves. The numerical results for the three-dimensional case (obtained with an ADER-DG-$\mathbb{P}4$ scheme) are depicted in Fig. 10, from which the same conclusions as in the 2D case can be drawn.

In order to assess the computational overhead of our new limiter, we run a mild version of the 2D explosion problem that can be successfully computed also with an *unlimited* version of the ADER-DG method. The inner state is given by $\rho = p = 1$, while the outer state is $\rho = p = 0.5$. The velocity is $\mathbf{v} = 0$ everywhere. The problem is run on the same mesh as before, using an ADER-DG $\mathbb{P}3$ scheme. The first simulation is performed with the unlimited version of the scheme and the second one with the *a posteriori* subcell limiter. Compared to the unlimited scheme, the total CPU time was increased by 50% when the limiter was active.

4.1.7. Mach 3 flow over a sphere

As a last example for the compressible Euler equations, we solve the problem of a Mach 3 flow over a sphere. The computational domain consists of an inner sphere of radius $R = 0.5$, at which no-slip wall boundary conditions are applied, and an outer sphere or radius $R = 1$, at the left of which a uniform flow of density $\rho = \gamma$, $\mathbf{v} = (3, 0, 0)$ and $p = 1$ is imposed. The right outflow boundary is obtained by subtracting a sphere of radius $R = 3$, centered in $\mathbf{x} = (3, 0, 0)$ from the previous configuration. The computational grid is composed of 341583 tetrahedral elements of characteristic mesh spacing $h = 0.033$. A sketch of the 3D mesh, together with the troubled cells highlighted in red is plotted in the top left panel of Fig. 11. Furthermore, a cut through the numerical solution in the plane $z = 0$ is drawn, where the distribution of troubled

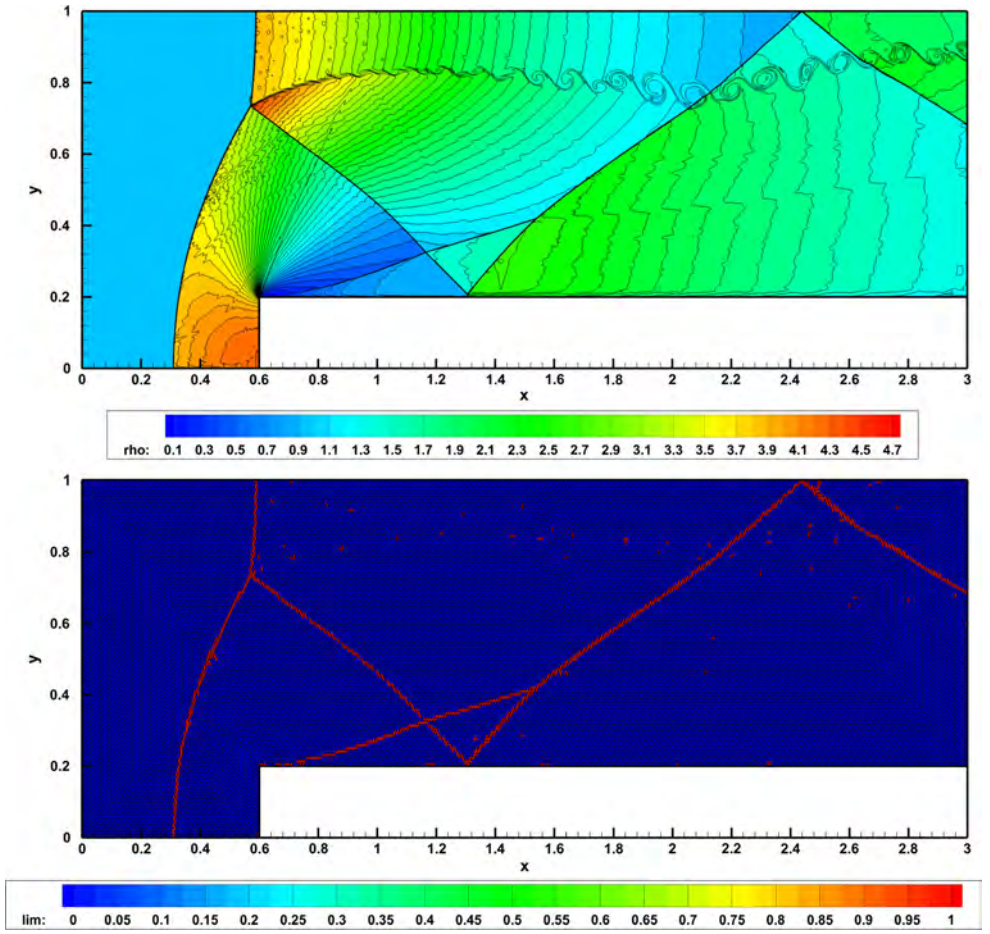

Fig. 8. Forward facing step problem obtained with the ADER-DG $\mathbb{P}_4$ scheme and *a posteriori* sub-cell finite volume limiter at time $t = 4.0$ on a grid with mesh spacing $h = 1/100$. Top: density contour lines. Bottom: troubled zones highlighted in red. (For interpretation of the references to color in this figure legend, the reader is referred to the web version of this article.)

cells, as well as the contour levels for density and pressure are drawn. We can observe a very sharp resolution of the shock wave.

4.2. The ideal magneto-hydrodynamics equations (MHD)

In this section we present the results obtained for the classical ideal MHD system that reads

$$\frac{\partial}{\partial t}\begin{pmatrix}\rho\\ \rho\mathbf{v}\\ \rho E\\ \mathbf{B}\\ \psi\end{pmatrix}+\nabla\cdot\begin{pmatrix}\rho\mathbf{v}\\ \rho\mathbf{v}\otimes\mathbf{v}+\left(p+\frac{1}{8\pi}\mathbf{B}^2\right)\mathbf{I}-\frac{1}{4\pi}\mathbf{B}\otimes\mathbf{B}\\ \left[\left(\rho E+p+\frac{1}{8\pi}\mathbf{B}^2\right)\mathbf{I}-\frac{1}{4\pi}\mathbf{B}\otimes\mathbf{B}\right]\cdot\mathbf{v}\\ \mathbf{B}\otimes\mathbf{v}-\mathbf{v}\otimes\mathbf{B}+\psi\mathbf{I}\\ c_h^2\mathbf{B}\end{pmatrix}=0, \tag{36}$$

where again the ideal gas EOS is used:

$$p=(\gamma-1)\left(\rho E-\frac{1}{2}\rho\mathbf{v}^2-\frac{1}{8\pi}\mathbf{B}^2\right). \tag{37}$$

Like in the case of the compressible Euler equations, ρ denotes the fluid density, $\mathbf{v}$ is the velocity vector, p is the fluid pressure and ρE is the total energy density; the magnetic field is denoted by $\mathbf{B}$. The PDE system (36) is the so-called *augmented* MHD system, which arises from the hyperbolic divergence-cleaning approach of Dedner et al. [38] and Kemm [91] that is needed to satisfy the constraint $\nabla\cdot\mathbf{B}=0$ approximately at the discrete level. For a detailed explanation of the origin of such divergence errors in the context of resonant hyperbolic PDE systems, see the recent paper by Kemm [90].

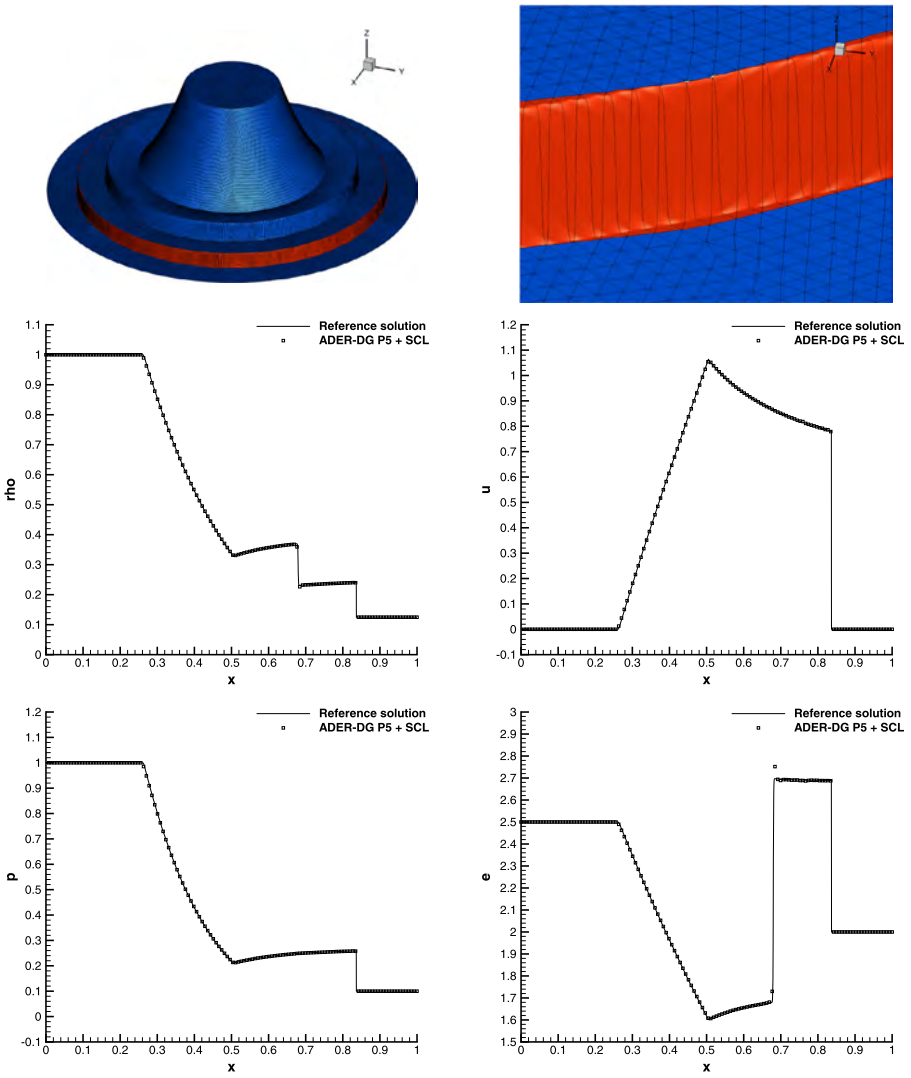

Fig. 9. Cylindrical explosion problem in 2D obtained with the ADER-DG $\mathbb{P}_5$ scheme and *a posteriori* sub-cell finite volume limiter at time $t = 0.2$ on a grid with mesh spacing $h = 1/100$. Top row left: 3D view of the density, computational grid and troubled cells in red. Top row right: zoom into the circular shock front. One can clearly see that the shock is well resolved within a single grid cell. Middle and bottom rows: 1D cut through the numerical solution for density, velocity, pressure and internal energy along the x-axis. (For interpretation of the references to color in this figure legend, the reader is referred to the web version of this article.)

The divergence cleaning is achieved by the scalar ψ, which transports divergence errors with the artificial speed c_h, so that they cannot accumulate locally. For alternative *exactly* divergence-free schemes for the MHD equations see, for example, [8,5,67,68,9,16,13]. For this system of PDEs the PAD criteria are the positivity of density and pressure which is not always obvious to maintain due to the presence of magnetic pressure in (37).

4.2.1. Smooth MHD vortex in 3D

For the numerical convergence studies in 3D, we solve a 3D version of the vortex test problem proposed by Balsara in [5]. The computational domain is given by the box $\Omega = [0; 12]^2 \times [0; 5]$ and six periodic boundary conditions are imposed on the domain boundaries. The initial condition is given in terms of the vector of primitive variables $\mathbf{V} = (\rho, u, v, w, p, B_x, B_y, B_z, \Psi)^T$ as

$$\mathbf{V}(\mathbf{x}, 0) = (1, 1 + \delta u, 1 + \delta v, 0, 1 + \delta p, \delta B_x, \delta B_y, \delta B_z, 0)^T, \tag{38}$$

with $\delta\mathbf{v} = (\delta u, \delta v, \delta w)^T$, $\delta\mathbf{B} = (\delta B_x, \delta B_y, \delta B_z)^T$ and

$$\delta\mathbf{v} = \frac{\kappa}{2\pi} e^{q(1-r^2)} \mathbf{e}_z \times \mathbf{r} \quad \delta\mathbf{B} = \frac{\mu}{2\pi} e^{q(1-r^2)} \mathbf{e}_z \times \mathbf{r}, \quad \delta p = \frac{1}{64 q \pi^3} \left(\mu^2 (1 - 2qr^2) - 4\kappa^2 \pi \right) e^{2q(1-r^2)}. \tag{39}$$

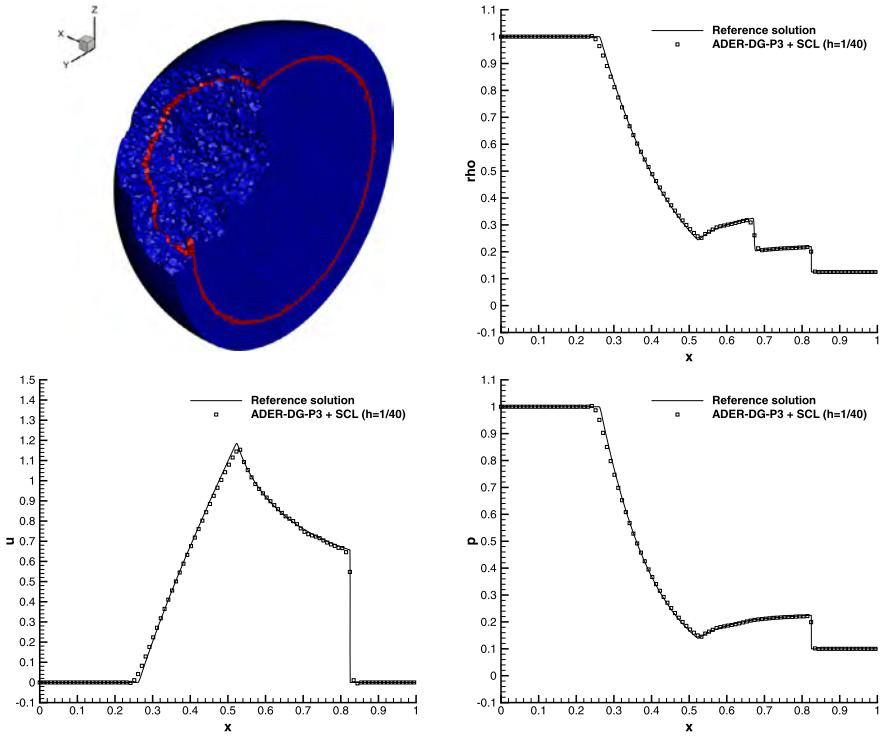

Fig. 10. Spherical explosion problem at time $t = 0.2$ obtained with an ADER-DG $\mathbb{P}3$ scheme and second order sub-cell limiter on an unstructured tetrahedral mesh with characteristic grid spacing $h = 1/40$. Top left: visualization of the mesh and troubled cells in red. From top right to bottom right: 1D cuts along the x-axis for the density, radial velocity and pressure and comparison with the reference solution. (For interpretation of the references to color in this figure legend, the reader is referred to the web version of this article.)

Table 5
L^1, L^2 and L^∞ errors and convergence rates for the smooth MHD vortex problem in 3D for the ADER-DG-$\mathbb{P}_N$ scheme with sub-cell limiter for variable B_x at time $t = 1$.

Smooth MHD vortex in 3D – ADER-DG-$\mathbb{P}_N$ + FV SCL									
	N_x	L^1 error	L^2 error	L^∞ error	L^1 order	L^2 order	L^∞ order	Theor.	d.o.f.
DG-$\mathbb{P}_2$	20	1.0569E−01	1.2108E−02	1.3865E−02	–	–	–	3	196,750
	30	2.6567E−02	3.1828E−03	5.5850E−03	3.41	3.30	2.24		815,500
	40	1.2517E−02	1.4869E−03	1.7923E−03	2.62	2.65	3.95		1,788,400
	50	5.7136E−03	6.8001E−04	8.1444E−04	3.51	3.51	3.53		4,016,140
DG-$\mathbb{P}_3$	20	9.6921E−03	1.2163E−03	3.0772E−03	–	–	–	4	393,500
	30	1.4881E−03	1.6858E−04	3.4896E−04	4.62	4.87	5.37		1,631,000
	40	6.3081E−04	6.2895E−05	1.5494E−04	2.98	3.43	2.82		3,576,800
	50	3.1697E−04	2.5875E−05	7.8888E−05	3.08	3.98	3.03		8,032,280
DG-$\mathbb{P}_4$	12	8.2485E−03	1.0673E−03	2.7461E−03	–	–	–	5	166,320
	20	1.0056E−03	1.1289E−04	3.5442E−04	4.12	4.40	4.01		688,625
	30	2.3827E−04	1.8876E−05	7.9228E−05	3.55	4.41	3.69		2,854,250

We have $\mathbf{e}_z = (0, 0, 1)$, $\mathbf{r} = (x - 5, y - 5, 0)$ and $r = \|\mathbf{r}\| = \sqrt{(x-5)^2 + (y-5)^2}$. The divergence cleaning speed is chosen as $c_h = 3$. The other parameters are $q = \frac{1}{2}$, $\kappa = 1$ and $\mu = \sqrt{4\pi}$, according to [5]. Simulations are run until the final time $t = 1$, where the exact solution is given by the initial condition shifted by $(1, 1)$ along the x and y axis, respectively. A representative tetrahedral mesh is depicted in Fig. 12, together with the pressure and B_y contour surfaces. The obtained convergence rates are listed in Table 5, showing that the ADER-DG method with *a posteriori* subcell limiter achieves its designed order of accuracy well also on three-dimensional unstructured tetrahedral meshes.

4.2.2. 3D MHD field loop

This problem consists of a cylindrical loop of magnetic field with a very low magnetic pressure compared to the gas pressure. The magnetic pressure is constant inside the loop and falls abruptly to zero at the loop's boundary which is initially set up at a radius of 0.3 units. The details of the set-up are described in Gardiner and Stone [67] and are not repeated here. The computational domain is given by the cube $\Omega = [-0.5; 0.5]^3$, where six periodic boundary conditions

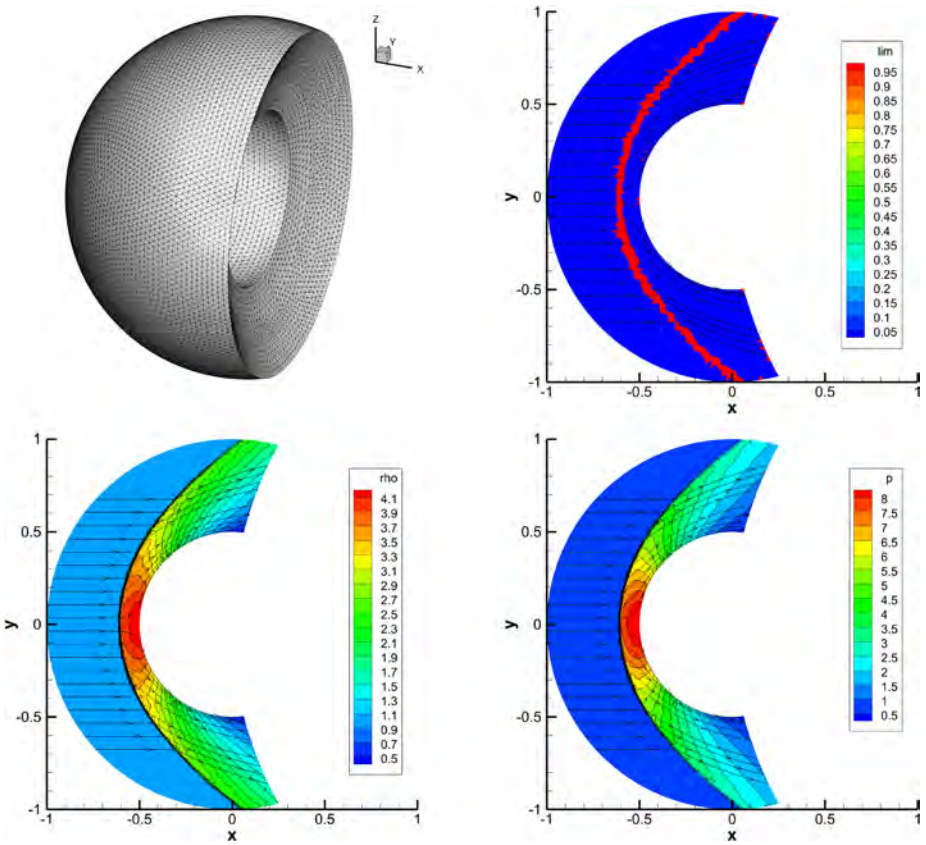

Fig. 11. Mach 3 flow over a sphere at time $t = 1.0$ obtained with an ADER-DG $\mathbb{P}3$ scheme and second order finite volume sub-cell limiter. Top left: visualization of the 3D mesh. From top right to bottom right: 2D cuts in the x–y plane showing the troubled cells, the density and the pressure distribution. (For interpretation of the references to color in this figure, the reader is referred to the web version of this article.)

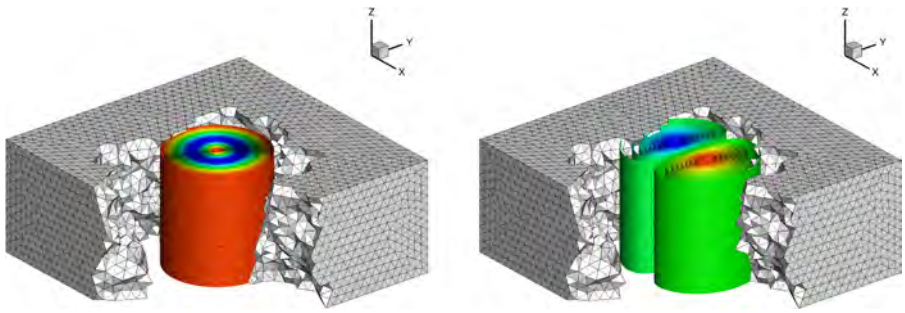

Fig. 12. Smooth MHD vortex problem at time $t = 1.0$ obtained with an ADER-DG $\mathbb{P}3$ scheme and second order sub-cell finite volume limiter on an unstructured tetrahedral mesh with $h = 12/30$. Left: pressure contour surfaces. Right: contour surfaces of the magnetic field component B_y.

have been imposed. The divergence cleaning speed is set to $c_h = 3$, and the problem is run to a final time of $t = 1.0$ with a fourth order ADER-DG-$\mathbb{P}4$ scheme and second order TVD sub-cell finite volume limiter. At the final time, the loop has been advected for one period, so that it must return to its initial location. The characteristic mesh size was $h = 1/25$, leading to a total number of 132745 tetrahedral elements, see also Fig. 13 for a view of the unstructured mesh and for a contour plot of the magnitude of the magnetic field. In the case of an unstructured tetrahedral mesh, the field loop is in general not aligned with the element faces, hence it is not necessary to tilt the 3D field loop as suggested in [68] for the case of a simple Cartesian grid. A two-dimensional cut through our computational results is presented in the right panel of Fig. 13. We find that the isotropic shape of the field loop is perfectly preserved after one periodic passage through the computational domain. Similar results have been obtained very recently with an exactly divergence-free ADER-WENO finite volume scheme in [13], but on a much finer mesh. We find that for this problem, the sub-cell limiter is activated only in the beginning of the simulation. Once the solution (which consists in the propagation of a linearly degenerate wave field) has been sufficiently smeared, it is propagated with the *unlimited* scheme for the rest of the simulation.

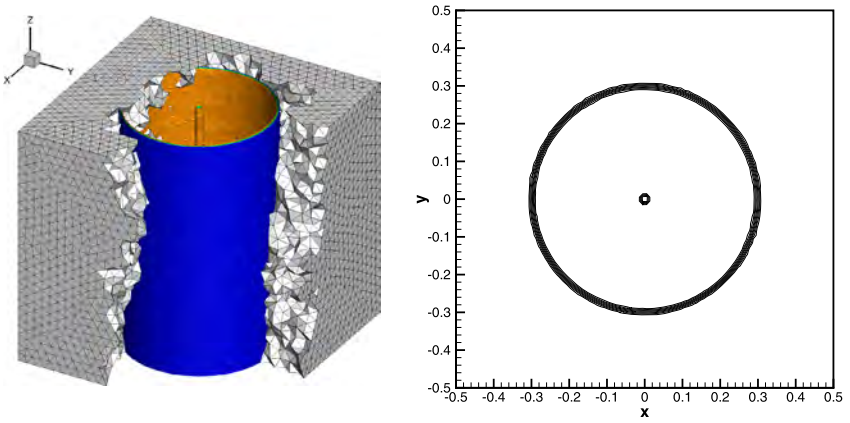

Fig. 13. 3D MHD field loop problem after one advection period at time $t = 1.0$ obtained with an ADER-DG $\mathbb{P}4$ scheme and second order sub-cell limiter on a coarse unstructured tetrahedral mesh with $h = 1/25$. Left: contour surfaces of the magnetic field strength. Right: contour lines of the magnetic field strength within the 2D cut plane $z = 0$.

4.2.3. Orszag–Tang vortex system

We now consider the well-known vortex system of Orszag and Tang [108], see also [111] and [37] for more details on the physics of the problem. Let us recall the setup of the problem: the computational domain is $\Omega = [0; 2\pi]^2$, the same parameters of the computation of Jiang and Wu [82] are used, however, scaling the magnetic field by $\sqrt{4\pi}$ due to the different normalization of the governing equations. The initial condition of the problem is given by

$$\left(\rho, u, v, p, B_x, B_y\right) = \left(\gamma^2, -\sin(y), \sin(x), \gamma, -\sqrt{4\pi}\sin(y), \sqrt{4\pi}\sin(2x)\right), \tag{40}$$

with $w = B_z = 0$ and $\gamma = \frac{5}{3}$. The final time is $t_{\text{final}} = 3.0$ and the divergence cleaning speed is set to $c_h = 2.0$, see [47]. We use an ADER-DG $\mathbb{P}_4$ scheme with second order *a posteriori* finite volume sub-cell limiter. The unstructured triangular mesh consists of 90126 elements with characteristic mesh spacing $h = \frac{2\pi}{200}$. In Fig. 14 the results are reported at different output times $t = 0.5, 2.0$ and 3.0. The pressure contour levels are plotted on the left, while the troubled zones are highlighted in red on the right. Unlimited cells are by convention shown in blue. On can observe that the limiter is mainly activated only when and where the shock waves start to form, while in the rest of the domain the unlimited DG scheme is used. The computational results agree qualitatively well with those presented elsewhere in the literature, see e.g. [82,47,61,100,143, 13].

4.2.4. MHD rotor problem

This last MHD test case is the classical MHD rotor problem proposed by Balsara and Spicer in [8]. It consists of a rapidly rotating fluid of high density embedded in a fluid at rest with low density. Both fluids are subject to an initially constant magnetic field. The rotor produces torsional Alfvén waves that are launched into the outer fluid at rest, resulting in a decrease of angular momentum of the spinning rotor. The computational domain Ω is a circle with radius $r = \frac{1}{2}$, the density inside the rotor is $\rho = 10$ for $0 \le r \le 0.1$ while the density of the ambient fluid at rest is set to $\rho = 1$. The rotor has an angular velocity of $\omega = 10$. The pressure is $p = 1$ and the magnetic field vector is set to $\mathbf{B} = (2.5, 0, 0)^T$ in the entire domain. As proposed by Balsara and Spicer we apply a linear taper to the velocity and to the density in the range from $0.1 \le r \le 0.105$ so that density and velocity match those of the ambient fluid at rest at a radius of $r = 0.105$. The speed for the hyperbolic divergence cleaning is set to $c_h = 2$ and $\gamma = 1.4$ is used. Transmissive boundary conditions are applied at the outer boundaries of the disk. We use an unstructured triangular mesh composed of 71046 triangles of characteristic size $h = 1/200$. The computational results obtained with the ADER-DG-$\mathbb{P}4$ scheme supplemented with second order *a posteriori* sub-cell finite volume limiter are displayed in Fig. 15. The results for the logarithm of the density, the pressure, the flow Mach number and for the magnetic pressure ($|\mathbf{B}|^2/(8\pi)$) are presented. We also show the troubled cells in red, while unlimited cells are depicted in blue.

Overall, we find a good agreement of our computational results with those obtained by standard WENO finite volume schemes published previously in the literature, see e.g. [47,61,100,143,13]. Further research will concern the extension of the present DG scheme to exactly divergence-free MHD based on the genuinely multi-dimensional Riemann solvers forwarded in [11,10,15,12,14] and using the novel constrained L_2 projection technique recently proposed in [13] for the finite volume context.

4.3. The seven equation Baer–Nunziato model

As last prototype PDE system of this paper we now consider the full seven-equation Baer–Nunziato model for compressible two-phase flows. The original model has been described in [4] and has been successively modified in [121,122].

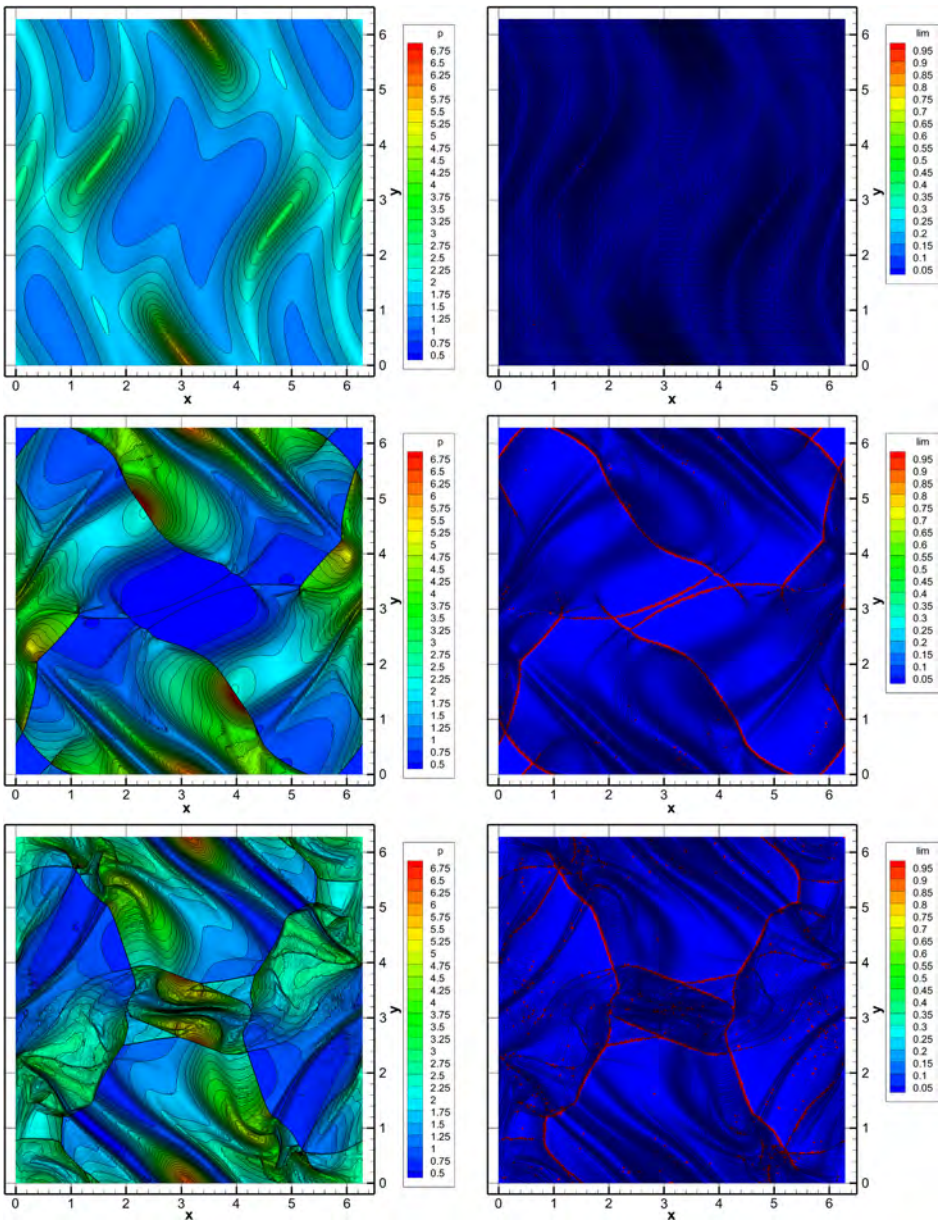

Fig. 14. Orszag–Tang vortex system at times $t = 0.5$, $t = 2.0$ and $t = 3.0$ from top to bottom. ADER-DG $\mathbb{P}_5$ solution, supplemented with the second order TVD *a posteriori* sub-cell finite volume limiter (left) and detected troubled zones in red (right). (For interpretation of the references to color in this figure legend, the reader is referred to the web version of this article.)

It has also been subsequently reduced to a five equation model, see [88,106]. The original Baer–Nunziato model has been proposed for the description of the deflagration–detonation transition in high-energy reactive materials composed of solid powder and compressible gas. The homogeneous model without relaxation terms [3,124,39,106] is given by the following non-conservative hyperbolic PDE system:

$$\frac{\partial}{\partial t}\left(\phi_1\rho_1\right) + \nabla\cdot\left(\phi_1\rho_1\mathbf{u}_1\right) = 0,$$

$$\frac{\partial}{\partial t}\left(\phi_1\rho_1\mathbf{u}_1\right) + \nabla\cdot\left(\phi_1\left(\rho_1\mathbf{u}_1\otimes\mathbf{u}_1 + p_1\mathbf{I}\right)\right) - p_I\nabla\phi_1 = 0,$$

$$\frac{\partial}{\partial t}\left(\phi_1\rho_1E_1\right) + \nabla\cdot\left[\phi_1\left(\rho_1E_1 + p_1\right)\mathbf{u}_1\right] - p_I\mathbf{u}_I\cdot\nabla\phi_1 = 0,$$

$$\frac{\partial}{\partial t}\left(\phi_2\rho_2\right) + \nabla\cdot\left(\phi_2\rho_2\mathbf{u}_2\right) = 0,$$

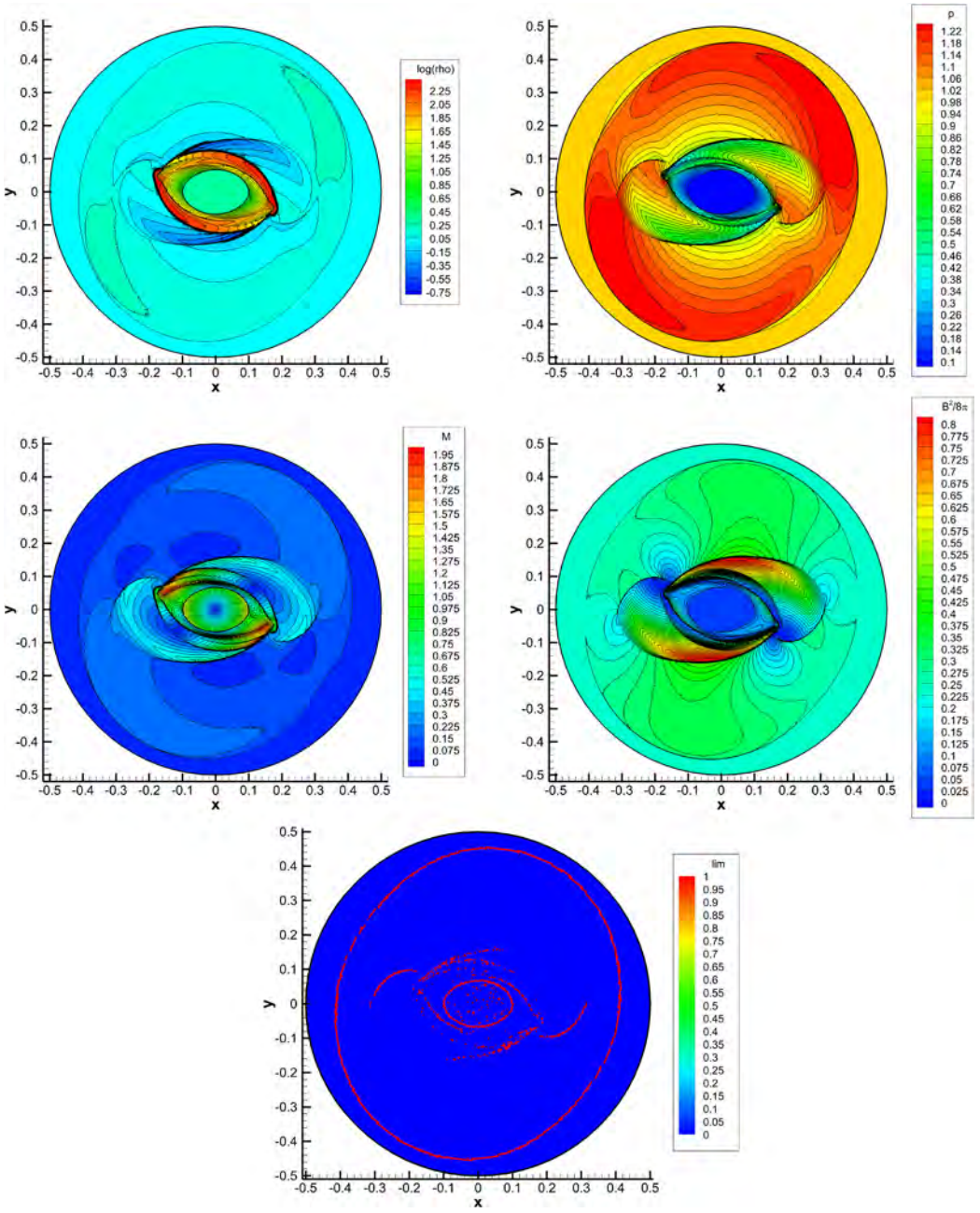

Fig. 15. MHD rotor problem at time $t = 0.25$. ADER-DG $\mathbb{P}_4$ solution with the second order TVD *a posteriori* sub-cell finite volume limiter for the logarithm of the fluid density, the pressure, the Mach number and the magnetic pressure. In the last row, the troubled zones are highlighted in red. (For interpretation of the references to color in this figure legend, the reader is referred to the web version of this article.)

$$\frac{\partial}{\partial t}\left(\phi_2 \rho_2 \mathbf{u}_2\right) + \nabla \cdot \left(\phi_2 \left(\rho_2 \mathbf{u}_2 \otimes \mathbf{u}_2 + p_2 \mathbf{I}\right)\right) - p_I \nabla \phi_2 = 0,$$
$$\frac{\partial}{\partial t}\left(\phi_2 \rho_2 E_2\right) + \nabla \cdot \left[\phi_2 \left(\rho_2 E_2 + p_2\right) \mathbf{u}_2\right] - p_I \mathbf{u}_I \cdot \nabla \phi_2 = 0,$$
$$\frac{\partial}{\partial t}\phi_1 + \mathbf{u}_I \cdot \nabla \phi_1 = 0. \tag{41}$$

In the above PDE system ϕ_j denotes the volume fraction of phase number j, with $j \in \{1, 2\}$, and the constraint $\phi_1 + \phi_2 = 1$. Furthermore, ρ_j, $\mathbf{u}_j$, p_j and $\rho_j E_j$ represent the density, the velocity vector, the pressure and the total energy per unit mass

Table 6
L^1, L^2 and L^∞ errors and convergence rates for the smooth Baer–Nunziato vortex problem [52] obtained with ADER-DG schemes with *a posteriori* sub-cell finite volume limiter at time $t = 2$. The errors refer to variable ϕ_1.

Smooth 2D Baer–Nunziato vortex problem – ADER-DG-$\mathbb{P}_N$ + FV SCL								
	N_x	L^1 error	L^2 error	L^∞ error	L^1 order	L^2 order	L^∞ order	Theor.
DG-$\mathbb{P}_3$	24	2.9428E–02	1.1718E–02	1.0068E–02	–	–	–	4
	32	2.6424E–04	8.1347E–05	1.2588E–04	16.38	17.28	15.23	
	48	4.6571E–05	1.5193E–05	2.2233E–05	4.28	4.14	4.28	
	64	1.6889E–05	5.9332E–06	9.2907E–06	3.97	3.78	3.76	
DG-$\mathbb{P}_4$	24	1.5939E–04	5.4366E–05	6.7999E–05	–	–	–	5
	32	3.6541E–05	1.2716E–05	2.0095E–05	5.12	5.05	4.24	
	48	4.3223E–06	1.6711E–06	3.3502E–06	5.26	5.01	4.42	
	64	1.4799E–06	5.8274E–07	9.6081E–07	4.63	4.45	4.39	
DG-$\mathbb{P}_5$	16	2.7355E–04	9.0657E–05	1.0641E–04	–	–	–	6
	24	2.3116E–05	8.3831E–06	1.7414E–05	6.09	5.87	4.46	
	32	3.9657E–06	1.4187E–06	2.1749E–06	6.13	6.18	7.23	
	48	3.3575E–07	1.2498E–07	2.6538E–07	6.09	5.99	5.19	
DG-$\mathbb{P}_6$	12	3.1351E–02	1.0422E–02	1.0378E–02	–	–	–	7
	16	5.8658E–05	2.1372E–05	2.7652E–05	21.83	21.52	20.61	
	24	4.8862E–06	1.7490E–06	2.1503E–06	6.13	6.17	6.30	
	32	8.1213E–07	1.7858E–07	2.5471E–07	6.24	7.93	7.42	

for phase number j, respectively. Alternatively, the first phase is also called the solid phase (index s) and the second phase the gas phase (index g), respectively.

The model (41) is closed by the stiffened gas equation of state (EOS) for each phase

$$e_j = \frac{p_j + \gamma_j \pi_j}{\rho_j(\gamma_j - 1)}, \tag{42}$$

and the definition of the total energy density

$$\rho_j E_j = \rho_j e_j + \frac{1}{2}\rho_j \mathbf{u}_j^2, \tag{43}$$

where γ_j is the ratio of specific heats and π_j is a material constant. In this paper, we choose $\mathbf{u_I} = \mathbf{u_1}$ for the interface velocity and the interface pressure is assumed to be $p_I = p_2$. This corresponds to the original choice proposed in [4] and which has also been adopted in [3,124,39,52,59,53]. However, alternative choices are also possible, see [121,122]. For this system of PDEs the PAD criteria used in the detection procedure of our subcell limiter consider the positivity of partial densities and pressures. Partial volume fraction ϕ_1 is checked for boundedness so that $0 \le \phi_1 \le 1$.

4.3.1. Smooth vortex problem

To study the convergence of our high order DG scheme supplemented with *a posteriori* sub-cell finite volume limiter also in the non-conservative case, we first run the smooth Baer–Nunziato vortex problem first proposed in [52]. It admits a non-trivial exact solution of the time-dependent Baer–Nunziato system (41) that is smooth. It is therefore well suited for the purpose of a numerical convergence test. The details of the computational setup are given in [52] and are not repeated here. The computational domain is the square $\Omega = [-10; 10]^2$ on which four periodic boundary conditions have been applied. The final simulation time is $t = 2$, for which the exact solution is given by the initial condition shifted by $[2, 2]$ to the top and to the right. The numerical convergence results obtained for third to seventh order schemes are reported in Table 6. From the results one can conclude that the designed order of accuracy is also reached in the case of non-conservative PDE. Note that for this test problem the *a posteriori* limiter has detected a small number of troubled cells on some of the coarse meshes, while it does not detect any troubled cell on sufficiently fine meshes. That is the reason why for this test problem one can note a sudden decrease of the error between one grid resolution and the next one, leading to a spurious increase of the observed order of accuracy. Once the troubled zone detector starts to work properly, the method reaches its designed order as expected.

4.3.2. Riemann problems

In this section we run two Riemann problems for the Baer–Nunziato system, whose initial conditions are detailed in Table 7. The same problems have also been solved in [52,53,49,22] using high order WENO finite volume schemes on unstructured meshes, on space-time adaptive Cartesian grids (AMR) and on moving meshes, respectively.

For details on the exact Riemann solver of the homogeneous system (41) see the papers by Andrianov & Warnecke [3], Schwendeman et al. [124] and Deledicque & Papalexandris [39].

An unstructured mesh made of 2226 triangular elements with characteristic mesh spacing $h = 1/100$ has been used. In Figs. 16 and 17 the results of the ADER-DG-$\mathbb{P}_5$ scheme with second order *a posteriori* sub-cell finite volume limiter

Table 7
Initial condition for the two Riemann problems run for the Baer–Nunziato model. Left state (L) and the right state (R) are provided as well as model values for γ_k, π_k and the final time t_f.

	ρ_s	u_s	p_s	ρ_g	u_g	p_g	ϕ_s	t_f
RP1 [39]	$\gamma_s = 1.4$, $\pi_s = 0$, $\gamma_g = 1.4$, $\pi_g = 0$							
L	1.0	0.0	1.0	0.5	0.0	1.0	0.4	0.10
R	2.0	0.0	2.0	1.5	0.0	2.0	0.8	
RP2 [39]	$\gamma_s = 3.0$, $\pi_s = 100$, $\gamma_g = 1.4$, $\pi_g = 0$							
L	800.0	0.0	500.0	1.5	0.0	2.0	0.4	0.10
R	1000.0	0.0	600.0	1.0	0.0	1.0	0.3	

are presented. In both figures the mesh is shown, together with the troubled cells in red and the unlimited cells in blue. Furthermore, the volume fraction for phase 1, the density, the x velocity component and the pressure are shown for each phase in a 1D cut through the discrete solution $\mathbf{u}_h$ along the x axis. The exact 1D reference solution provided by [39] is also plotted for comparison. We observe that the troubled cells are properly detected in the vicinity of the shock waves in both phases. From the 1D plots one can note that the location of the waves, the flat plateaus and even the tiny waves are properly captured without spurious oscillations.

4.3.3. 2D cylindrical explosion problems

We use the same initial condition given for the Riemann problems in Table 7 to solve two cylindrical explosion problems with the compressible Baer–Nunziato model (41). The computational domain Ω is a circle of radius $R = 1$ that has been discretized with a characteristic mesh size of $h = 1/100$, leading to a total number of 68324 triangular elements. In all cases the initial state $\mathbf{Q}(\mathbf{x}, 0)$ is assigned by taking

$$\mathbf{Q}(\mathbf{x}, 0) = \begin{cases} \mathbf{Q}_i, & \text{if} \quad |\mathbf{x}| < r_c \\ \mathbf{Q}_o, & \text{else} \end{cases}, \tag{44}$$

with $r_c = 0.5$ representing the location of the initial discontinuity. The left state reported in Table 7 is assumed to be the inner state $\mathbf{Q}_i$, while the right state represents here the outer state $\mathbf{Q}_o$.

A radial reference solution can be obtained by solving an equivalent 1D balance law with geometric source terms, see [52] for all details. The computational results obtained with an ADER-DG-$\mathbb{P}_5$ scheme are reported together with the reference solution in Figs. 18 and 19. For problem EP1 we have employed the Osher-type method (13), while the second problem EP2 has been run with the new path-conservative extension of the HLLEM method proposed in [48]. As usual, troubled cells are highlighted in red, while unlimited cells are plotted in blue. One finds that all discontinuities are resolved very sharply, without spurious oscillations. The limiter is only activated in a few cells, mostly close to the shock waves in each phase. Some false positive activations of the limiter in smooth regions can be noted for the second problem in Fig. 19.

4.4. Nonconvex scalar problem

In this section we solve the non-convex scalar model problem proposed by Kurganov et al. in [95]. The governing PDE is given by

$$\frac{\partial u}{\partial t} + \frac{\partial \sin(u)}{\partial x} + \frac{\partial \cos(u)}{\partial y} = 0, \tag{45}$$

with initial data

$$u(\mathbf{x}, 0) = \begin{cases} 3.5, \pi & \text{if} \quad |\mathbf{x}| \leq 1, \\ 0.25, \pi & \text{if} \quad |\mathbf{x}| > 1. \end{cases} \tag{46}$$

The computational domain is a circle of radius $R = 2$, centered in $\mathbf{x}_c = (0, -0.5)$ and discretized with a rather coarse grid composed of 11056 triangles. Simulations are carried out with an ADER-DG $\mathbb{P}_3$ scheme up to a final time of $t = 1.0$. The simple Rusanov flux (11) has been used for this test problem. The computational results for u are depicted in Fig. 20, together with the limited cells in red and the unlimited cells in blue. One can observe that the numerical solution corresponds to the correct entropy solution identified in Kurganov et al. (see Fig. 5.9 left and Fig. 5.11 left in [95]), while second order TVD schemes with compressive limiters or higher order WENO schemes have been shown in [95] to converge to a *wrong* solution that does not satisfy the entropy principle. Our computational results confirm once more the accuracy and robustness of our simple high order ADER-DG scheme with *a posteriori* subcell TVD finite volume limiter also for this nontrivial test problem of a non-convex scalar conservation law. In particular, compared with Fig. 5.11 right in [95], our scheme needs less limiting.

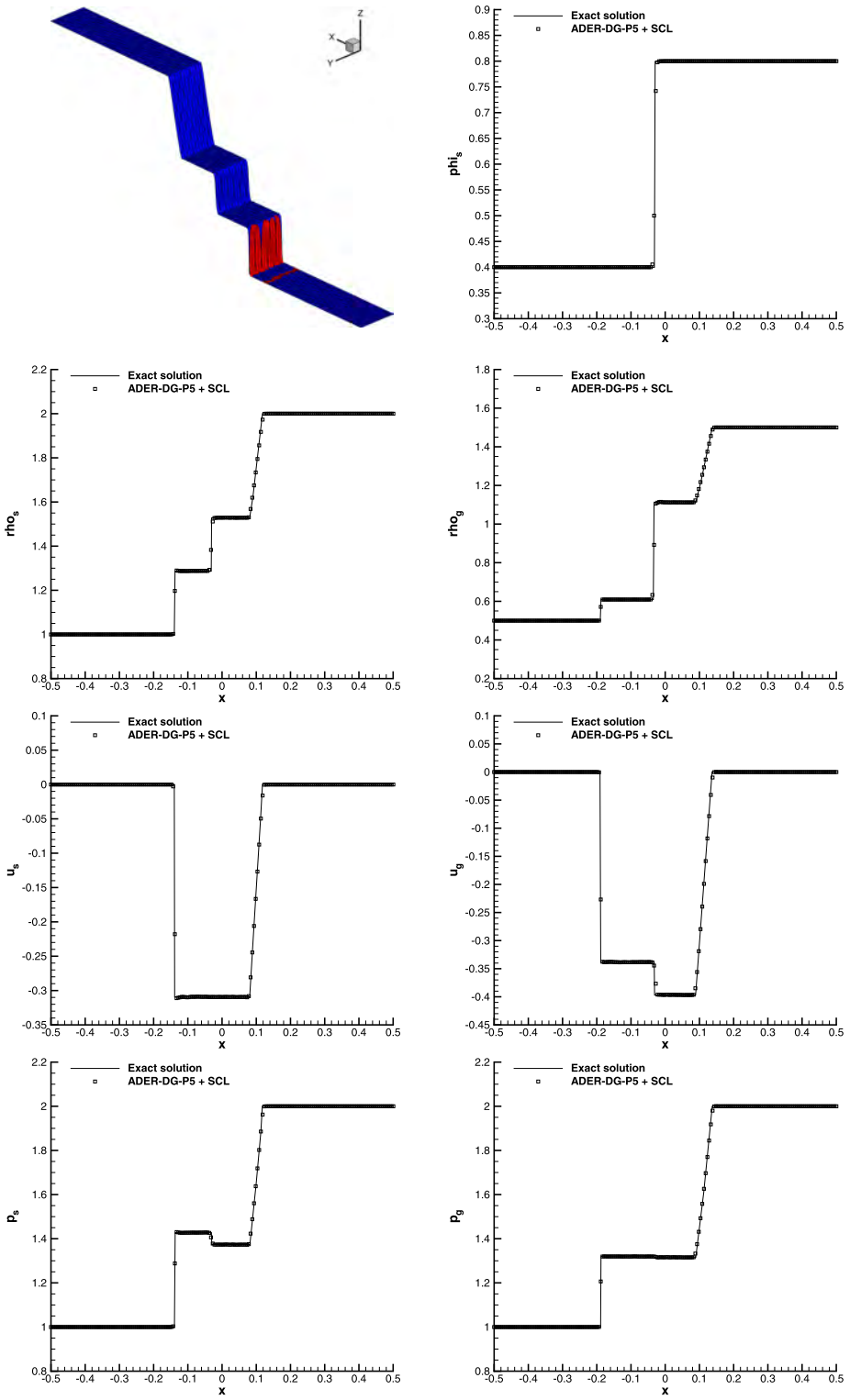

Fig. 16. Numerical results for Riemann problem RP1 of the seven-equation Baer–Nunziato model at time $t = 0.1$ and comparison with the exact solution – ADER-DG-$\mathbb{P}_5$ scheme with second order *a posteriori* sub-cell finite volume limiter. (For interpretation of the references to color in this figure, the reader is referred to the web version of this article.)

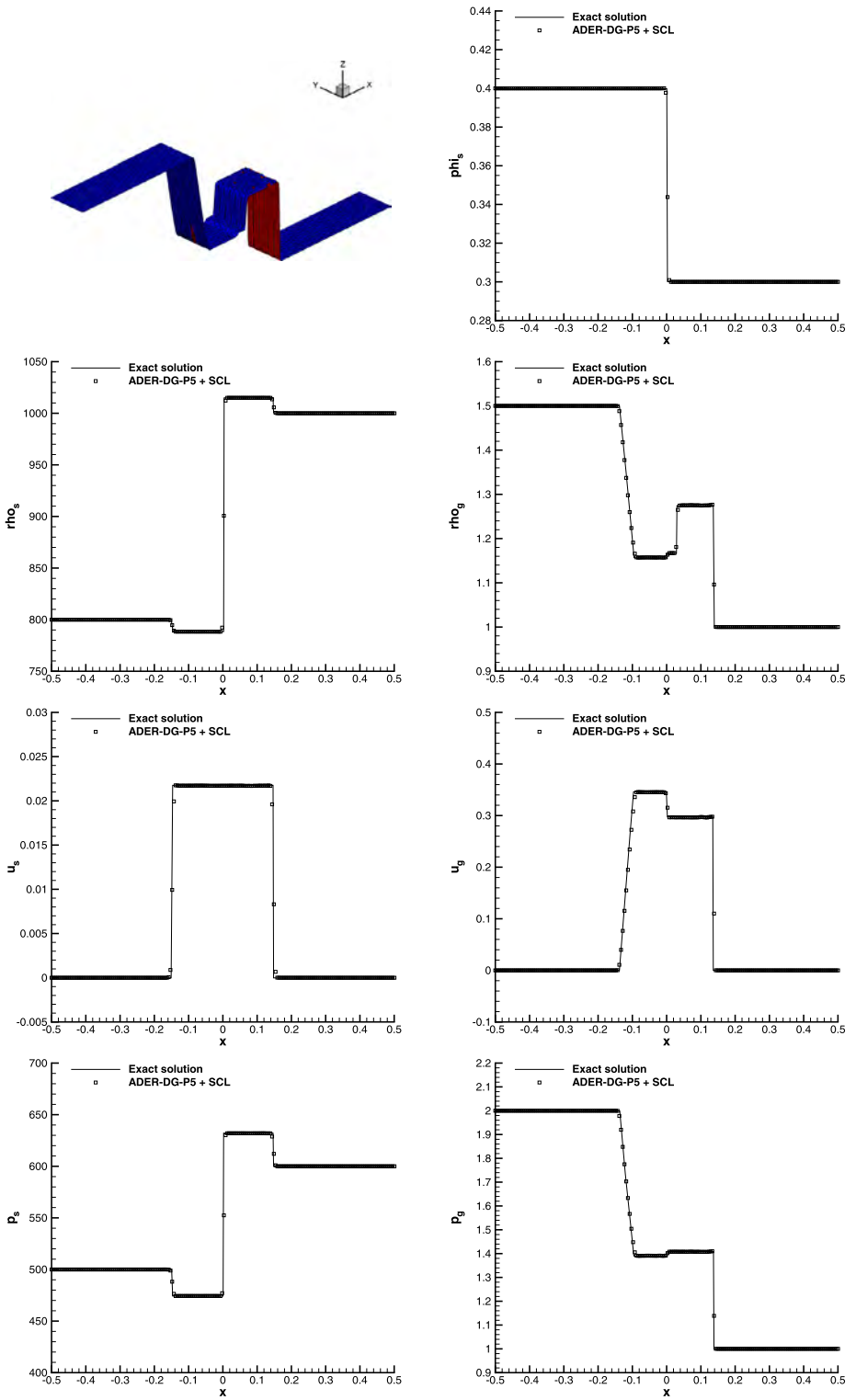

Fig. 17. Numerical results for Riemann problem RP2 of the seven-equation Baer–Nunziato model at time $t = 0.1$ and comparison with the exact solution – ADER-DG-$\mathbb{P}_5$ scheme with second order *a posteriori* sub-cell finite volume limiter. (For interpretation of the references to color in this figure, the reader is referred to the web version of this article.)

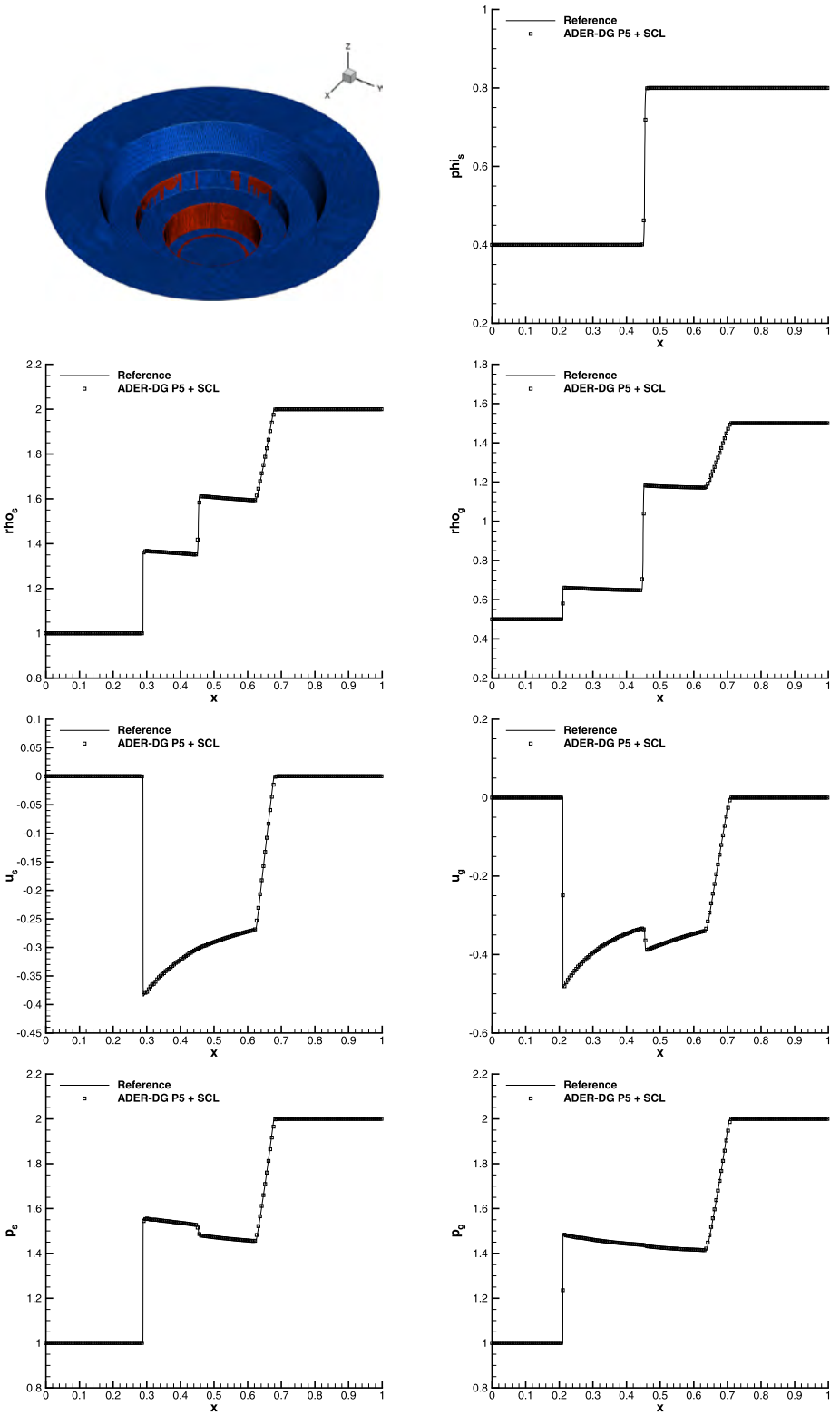

Fig. 18. Numerical results obtained with an ADER-DG-$\mathbb{P}_5$ scheme supplemented with second order *a posteriori* sub-cell finite volume limiter for the 2D explosion problem EP1 of the seven-equation Baer–Nunziato model at time $t = 0.15$ and comparison with the 1D reference solution. (For interpretation of the references to color in this figure, the reader is referred to the web version of this article.)

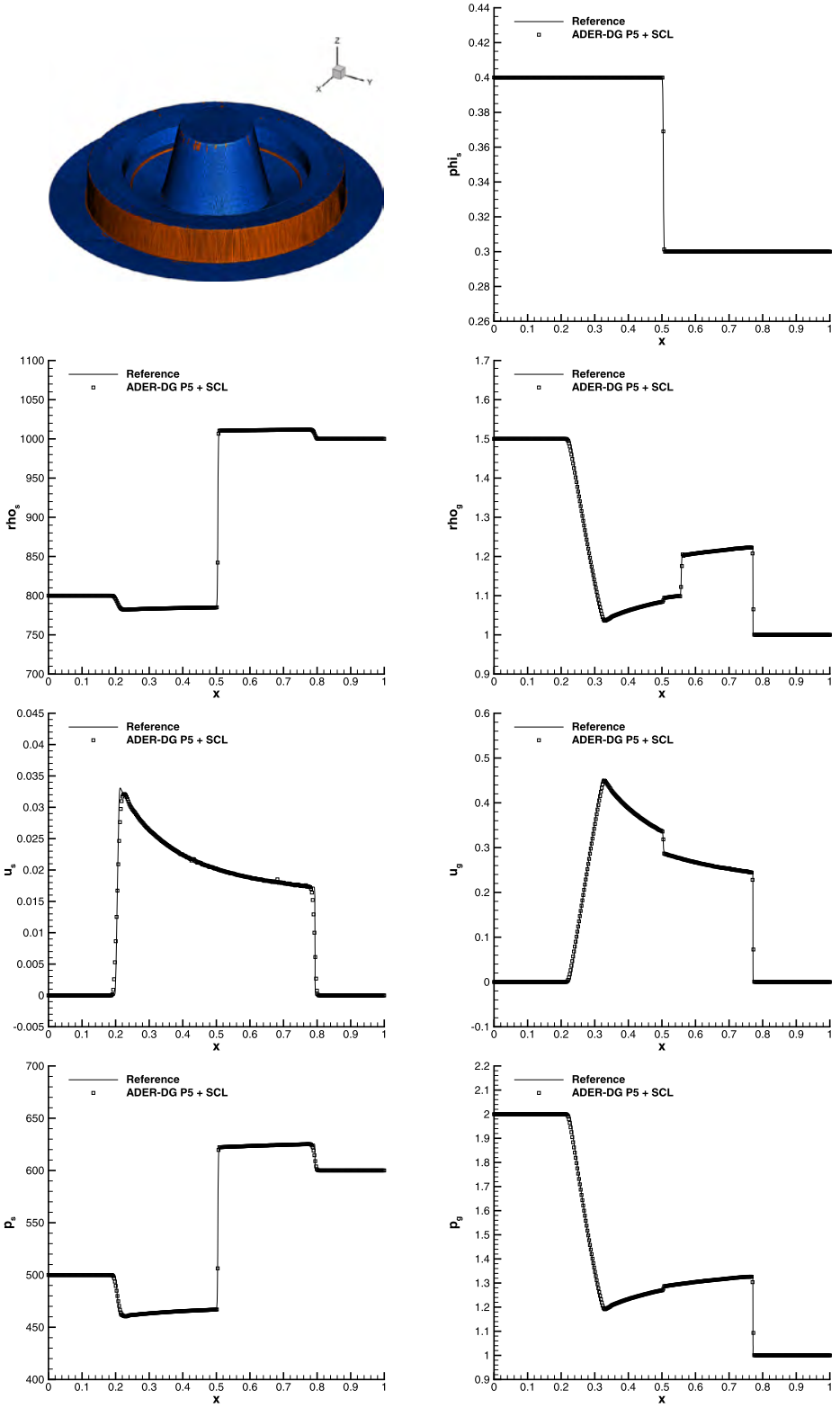

Fig. 19. Numerical results obtained with an ADER-DG-$\mathbb{P}_5$ scheme supplemented with second order *a posteriori* sub-cell finite volume limiter for the 2D explosion problem EP2 of the seven-equation Baer–Nunziato model at time $t = 0.2$ and comparison with the 1D reference solution. (For interpretation of the references to color in this figure, the reader is referred to the web version of this article.)

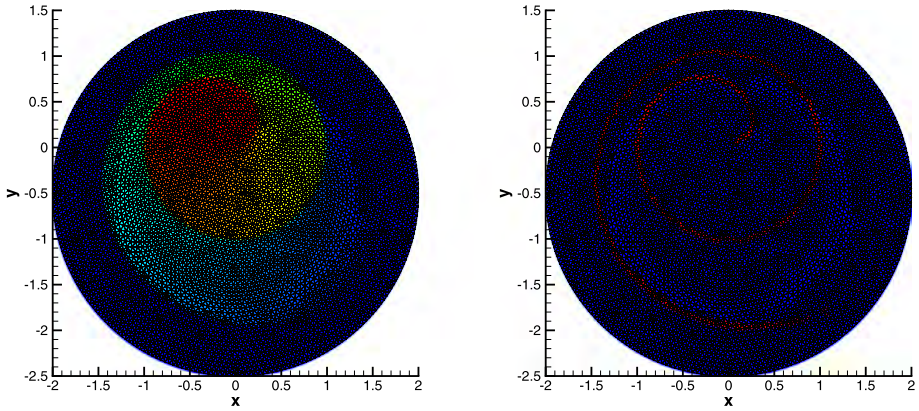

Fig. 20. Contour levels of u for the nonconvex scalar model problem of Kurganov et al. [95] (left) using an ADER-DG $\mathbb{P}_3$ scheme. Limited cells are highlighted in red and unlimited cells are highlighted in blue (right). (For interpretation of the references to color in this figure legend, the reader is referred to the web version of this article.)

5. Conclusion

In this paper we have presented a simple but very effective and accurate *a posteriori* sub-cell limiter of high order discontinuous Galerkin finite element methods for the solution of conservative and non-conservative hyperbolic systems of PDE on unstructured simplex meshes in two and three space dimensions. The new scheme directly derives from a previous method designed for fixed and adaptive Cartesian grids, see [62,143,142].

The main idea of our new limiter is to run first a classical unlimited DG scheme without any additional dissipative mechanism such as artificial viscosity, moment or (H)WENO-type limiters. This unlimited DG scheme will produce a so-called *candidate solution*. After the computation of the candidate solution a *detection phase* separates the valid cells, whose DG solution is acceptable, from the invalid troubled cells. This part of the algorithm is similar to the existing troubled-cell indicators of typical DG limiters. For the method proposed in this paper, the detection is based on physical criteria, like positivity of density and pressure, and on a relaxed discrete maximum principle in the sense of polynomials.

Within our new approach the candidate solution at time t^{n+1} in the troubled cells is then *discarded* and is subsequently *recomputed* by using once more the governing PDE system and by starting again from a valid discrete solution at the previous time t^n. This is different compared to classical (H)WENO- and moment-type limiters, where the limited solution in the troubled cells is obtained by a nonlinear *post-processing* of the given data at time t^{n+1}. The fact that we *go back* to a valid solution at the old time level and solve the PDE again with a more robust scheme on a sub-grid is the most important philosophical difference between our new *a posteriori* limiter and other existing limiters for the DG finite element method. In order to maintain the sub-grid resolution capability also in troubled cells, the DG polynomials at time t^n are projected onto a fine sub-grid and then evolved in time on the sub-grid level with a more robust finite volume scheme. Finally, the evolved sub-cell averages at time t^{n+1} are gathered back into a high order piecewise polynomial via a standard (unlimited) finite volume reconstruction, which completes the limiting procedure. If the same cell is detected as troubled also in the next time step, the sub-grid finite volume scheme starts over directly from the sub-cell averages obtained via the finite volume scheme in the previous time step, without projecting the (invalid) DG polynomial onto the sub-grid. This somewhat crude idea of *a posteriori* detection, and recomputation of certain troubled cells on a sub-grid with a more robust finite volume scheme is very simple to implement and has shown to be extremely powerful. Indeed, the philosophy of an *a posteriori* stabilization of the DG method is independent of the nominal order of accuracy of the scheme, the type of the mesh, the PDE system, the number of space dimensions and the chosen sub-cell finite volume scheme. On a large set of 2D and 3D test cases, we have shown that the DG method supplemented with *a posteriori* sub-cell stabilization seems to be a valid numerical tool for the solution of different nonlinear hyperbolic PDE systems, which include the Euler equations of compressible gas dynamics, the ideal magneto-hydrodynamics equations (MHD) and the Baer–Nunziato model of compressible multi-phase flows. In the present approach, rather large values of the polynomial degree N can be used for the approximation space of the discrete solution. In this work, approximation degrees from $N = 2$ up to $N = 6$ have been tested. Since the stabilization technique generally detects only very few troubled cells per time step, the extra cost induced by the necessary finite volume update of the sub-cell averages is acceptable. Due to the use of a fine sub-grid in the limiter, discontinuities are very well resolved even on a very coarse main grid if high values of N are used. For that very reason, the new limiter approach does *not* destroy the sub-cell resolution capabilities of the DG method, even in the presence of shock waves.

Moreover, the present ADER-DG scheme supplemented with *a posteriori* sub-cell finite volume limiter has not only been implemented on general unstructured meshes, but due to its locality and one-step time discretization it is also well suited for running on massively parallel supercomputers via MPI parallelization. This opens the door for a future use of this new family of schemes in the context of more complex applications in science and engineering.

Acknowledgements

The research presented in this paper has been financed by the European Research Council (ERC) under the European Union's Seventh Framework Programme (FP7/2007–2013) with the research project *STiMulUs*, ERC Grant agreement No. 278267.

The authors would like to acknowledge PRACE for awarding access to the SuperMUC supercomputer based in Munich, Germany at the Leibniz Rechenzentrum (LRZ).

Most of the material of this paper has been gathered while R.L. visited the University of Trento for three months. He would like to warmly acknowledge the financial support of CIMI, Université de Toulouse and the French National Research Agency (ANR) under project ANR-JS01-012-01 "ALE INC(ubator) 3D". The research was also partially supported by ANR-11-LABX-0040-CIMI within the program ANR-11-IDEX-0002-02.

Last but not least, the authors would like to thank the two anonymous referees for their constructive comments and remarks, which helped to improve the quality and clarity of this paper.

Appendix A. Best practice guideline for the transformation of an unlimited DG code into an *a posteriori* sub-cell stabilized DG code

In this appendix we describe the main actions that must be taken to transform a given DG code into a DG code that is stabilized with an *a posteriori* finite volume sub-cell limiter:

1. Within the existing DG code, remove any limiter or stabilization technique previously employed. As such, the DG scheme is run in its pure, unlimited form and produces the so-called candidate solution $\mathbf{u}_h^*$.
2. Implement a subroutine `Detection` which tests the cell centered DG solution $\mathbf{u}_h^*$ against appropriate detection criteria (depending on the system of PDEs solved). This routine produces the troubled-zones indicator β_i^{n+1} as a result, i.e. whether the DG polynomial in cell T_i is accepted, or not. If $\beta_i^{n+1} = 1$ the cell index i is added to a list of `TroubledCells`. The candidate solution in troubled cells is discarded whereas, for valid cells the solution is stored as final value $\mathbf{u}_h^{n+1}$. This ends the DG part of the scheme.
3. After having run the unlimited DG scheme and the detector, pick one cell index from the `TroubledCells` list, say i.
   - Implement a routine `Submesh` that creates a sub-mesh of cell T_i. The sub-mesh must be large enough ($N_s \geq N+1$), but preferably use $N_s = 2N+1$ sub-cells per spatial direction where N is the polynomial degree of the DG scheme.
   - Implement an L_2 projection `Scatter` of polynomials $\mathbf{u}_h^n$ onto this sub-mesh to get piecewise constant data $\mathbf{v}_{i,j}^n$, hence implement the operator $\mathbf{v}_h^n = \mathcal{P}(\mathbf{u}_h^n)$. In this manner, compute the initial and boundary data for the troubled cell i and its direct Neumann neighbors, according to (19).
   - Implement the sub-cell finite volume limiter `FVupdate`, i.e. the operator $\mathbf{v}_h^{n+1} = \mathcal{A}(\mathbf{v}_h^n)$. Here, for instance, a very simple first order Godunov-type scheme with Rusanov flux can be used to start with. Note that the timestep of the DG scheme can be used here, as the time steps resulting from the CFL condition of the DG scheme on the main grid and of the finite volume scheme on the sub-grid are alike. This FV scheme updates the sub-cell centered data to get $\mathbf{v}_{i,j}^{n+1}$ which are acceptable sub-cell solutions as provided by a stable and robust FV scheme.
   - Implement a routine `Gather` which computes a polynomial $\mathbf{u}_h^{n+1} = \mathcal{R}(\mathbf{v}_h^{n+1})$ that takes the sub-cell averages $\mathbf{v}_{i,j}^{n+1}$ as input and produces as output the degrees of freedom $\hat{\mathbf{u}}_{l,i}^{n+1}$ of the *limited* DG polynomial. The subroutine `Gather` is the inverse operator of the L_2 projection operator `Scatter`, since $\mathcal{R} \circ \mathcal{P} = \mathcal{I}$. This ends the timestep, since troubled cells have now been recomputed and stored into $\mathbf{u}_h^{n+1}$ with previously accepted cells from the DG scheme.
   - To obtain a conservative scheme, all Neumann neighbors of troubled cells T_i need to be corrected and must take into account that the fluxes across the neighbor edges have changed.

Note that in the `Detection` routine, the use of `Scatter` routine is mandatory to get a sub-cell based discrete maximum principle for the DG polynomials, see (26). As already mentioned in the core of this paper a first order finite volume scheme `FVupdate` is *de facto* equivalent to a DG scheme of first order of accuracy. As such there is no need to implement any new scheme if an unlimited DG scheme of arbitrary order of accuracy is already accessible.

References

[1] R. Abgrall, S. Karni, A comment on the computation of non-conservative products, J. Comput. Phys. 229 (2010) 2759–2763.
[2] A. Burbeau, P. Sagaut, C.H. Bruneau, A problem-independent limiter for high-order Runge–Kutta discontinuous Galerkin methods, J. Comput. Phys. 169 (1) (May 2001) 111–150.
[3] N. Andrianov, G. Warnecke, The Riemann problem for the Baer–Nunziato two-phase flow model, J. Comput. Phys. 212 (2004) 434–464.
[4] M.R. Baer, J.W. Nunziato, A two-phase mixture theory for the deflagration-to-detonation transition (DDT) in reactive granular materials, Int. J. Multiph. Flow 12 (1986) 861–889.
[5] D. Balsara, Second-order accurate schemes for magnetohydrodynamics with divergence-free reconstruction, Astrophys. J. Suppl. Ser. 151 (2004) 149–184.
[6] D. Balsara, C. Altmann, C.D. Munz, M. Dumbser, A sub-cell based indicator for troubled zones in RKDG schemes and a novel class of hybrid RKDG+HWENO schemes, J. Comput. Phys. 226 (2007) 586–620.

[7] D. Balsara, C.W. Shu, Monotonicity preserving weighted essentially non-oscillatory schemes with increasingly high order of accuracy, J. Comput. Phys. 160 (2000) 405–452.
[8] D. Balsara, D. Spicer, A staggered mesh algorithm using high order Godunov fluxes to ensure solenoidal magnetic fields in magnetohydrodynamic simulations, J. Comput. Phys. 149 (1999) 270–292.
[9] D.S. Balsara, T. Rumpf, M. Dumbser, C.-D. Munz, Efficient, high accuracy ADER-WENO schemes for hydrodynamics and divergence-free magnetohydrodynamics, J. Comput. Phys. 228 (April 2009) 2480–2516.
[10] D.S. Balsara, Multidimensional HLLE Riemann solver: application to Euler and magnetohydrodynamic flows, J. Comput. Phys. 229 (2010) 1970–1993.
[11] D.S. Balsara, A two-dimensional HLLC Riemann solver for conservation laws: application to Euler and magnetohydrodynamic flows, J. Comput. Phys. 231 (2012) 7476–7503.
[12] D.S. Balsara, Multidimensional Riemann problem with self-similar internal structure. Part I. Application to hyperbolic conservation laws on structured meshes, J. Comput. Phys. 277 (2014) 163–200.
[13] D.S. Balsara, M. Dumbser, Divergence-free MHD on unstructured meshes using high order finite volume schemes based on multidimensional Riemann solvers, J. Comput. Phys. 299 (2015) 687–715.
[14] D.S. Balsara, M. Dumbser, Multidimensional Riemann problem with self-similar internal structure. Part II. Application to hyperbolic conservation laws on unstructured meshes, J. Comput. Phys. 287 (2015) 269–292.
[15] D.S. Balsara, M. Dumbser, R. Abgrall, Multidimensional HLLC Riemann solver for unstructured meshes – with application to Euler and MHD flows, J. Comput. Phys. 261 (2014) 172–208.
[16] D.S. Balsara, C. Meyer, M. Dumbser, H. Du, Z. Xu, Efficient implementation of ADER schemes for Euler and magnetohydrodynamical flows on structured meshes – speed comparisons with Runge–Kutta methods, J. Comput. Phys. 235 (2013) 934–969.
[17] G.E. Barter, D.L. Darmofal, Shock capturing with PDE-based artificial viscosity for DGFEM: Part I. Formulation, J. Comput. Phys. 229 (5) (March 2010) 1810–1827.
[18] T. Barth, P. Charrier, Energy stable flux formulas for the discontinuous Galerkin discretization of first-order nonlinear conservation laws, Technical Report NAS-01-001, NASA, 2001.
[19] T.J. Barth, D.C. Jespersen, The design and application of upwind schemes on unstructured meshes, AIAA Paper 89-0366, 1989, pp. 1–12.
[20] F. Bassi, S. Rebay, High-order accurate discontinuous finite element solution of the 2D Euler equations, J. Comput. Phys. 138 (1997) 251–285.
[21] T. Bolemann, M. Üffinger, F. Sadlo, T. Ertl, C.-D. Munz, Direct visualization of piecewise polynomial data, Notes Numer. Fluid Mech. Multidiscipl. Des. 128 (2015) 535–550.
[22] W. Boscheri, M. Dumbser, A direct arbitrary-Lagrangian–Eulerian ADER-WENO finite volume scheme on unstructured tetrahedral meshes for conservative and nonconservative hyperbolic systems in 3D, J. Comput. Phys. 275 (2014) 484–523.
[23] E. Casoni, J. Peraire, A. Huerta, One-dimensional shock-capturing for high-order discontinuous Galerkin methods, Int. J. Numer. Methods Fluids 71 (6) (2013) 737–755.
[24] M.J. Castro, J.M. Gallardo, A. Marquina, Approximate Osher–Solomon schemes for hyperbolic systems, Appl. Math. Comput. (2015), http://dx.doi.org/10.1016/j.amc.2015.06.104.
[25] M.J. Castro, J.M. Gallardo, C. Parés, High-order finite volume schemes based on reconstruction of states for solving hyperbolic systems with nonconservative products. Applications to shallow-water systems, Math. Comput. 75 (2006) 1103–1134.
[26] M.J. Castro, P.G. LeFloch, M.L. Muñoz-Ruiz, C. Parés, Why many theories of shock waves are necessary: convergence error in formally path-consistent schemes, J. Comput. Phys. 227 (2008) 8107–8129.
[27] J. Cesenek, M. Feistauer, Theory of the space-time discontinuous Galerkin method for nonstationary parabolic problems with nonlinear convection and diffusion, SIAM J. Numer. Anal. 50 (3) (2012) 1181–1206.
[28] S. Clain, S. Diot, R. Loubère, A high-order finite volume method for systems of conservation laws—multi-dimensional optimal order detection (MOOD), J. Comput. Phys. 230 (10) (2011) 4028–4050.
[29] B. Cockburn, S. Hou, C.W. Shu, The Runge–Kutta local projection discontinuous Galerkin finite element method for conservation laws IV: the multidimensional case, Math. Comput. 54 (1990) 545–581.
[30] B. Cockburn, G.E. Karniadakis, C.W. Shu, Discontinuous Galerkin Methods, Lecture Notes in Computational Science and Engineering, Springer, 2000.
[31] B. Cockburn, S.Y. Lin, C.W. Shu, TVB Runge–Kutta local projection discontinuous Galerkin finite element method for conservation laws III: one dimensional systems, J. Comput. Phys. 84 (1989) 90–113.
[32] B. Cockburn, C.W. Shu, TVB Runge–Kutta local projection discontinuous Galerkin finite element method for conservation laws II: general framework, Math. Comput. 52 (1989) 411–435.
[33] B. Cockburn, C.W. Shu, The Runge–Kutta local projection P1-discontinuous Galerkin finite element method for scalar conservation laws, Math. Model. Numer. Anal. 25 (1991) 337–361.
[34] B. Cockburn, C.W. Shu, The Runge–Kutta discontinuous Galerkin method for conservation laws V: multidimensional systems, J. Comput. Phys. 141 (1998) 199–224.
[35] B. Cockburn, C.W. Shu, Runge–Kutta discontinuous Galerkin methods for convection-dominated problems, J. Sci. Comput. 16 (2001) 173–261.
[36] A.W. Cook, W.H. Cabot, A high-wavenumber viscosity for high-resolution numerical methods, J. Comput. Phys. 195 (2) (April 2004) 594–601.
[37] R.B. Dahlburg, J.M. Picone, Evolution of the Orszag–Tang vortex system in a compressible medium. I. Initial average subsonic flow, Phys. Fluids B 1 (1989) 2153–2171.
[38] A. Dedner, F. Kemm, D. Kröner, C.-D. Munz, T. Schnitzer, M. Wesenberg, Hyperbolic divergence cleaning for the MHD equations, J. Comput. Phys. 175 (2002) 645–673.
[39] V. Deledicque, M.V. Papalexandris, An exact Riemann solver for compressible two-phase flow models containing non-conservative products, J. Comput. Phys. 222 (2007) 217–245.
[40] S. Diot, S. Clain, R. Loubère, Improved detection criteria for the multi-dimensional optimal order detection (MOOD) on unstructured meshes with very high-order polynomials, Comput. Fluids 64 (2012) 43–63.
[41] S. Diot, R. Loubère, S. Clain, The MOOD method in the three-dimensional case: very-high-order finite volume method for hyperbolic systems, Int. J. Numer. Methods Fluids 73 (2013) 362–392.
[42] D. Kuzmin, A vertex-based hierarchical slope limiter for p-adaptive discontinuous Galerkin methods, J. Comput. Appl. Math. 233 (12) (2010) 3077–3085.
[43] D. Kuzmin, Slope limiting for discontinuous Galerkin approximations with a possibly non-orthogonal Taylor basis, Int. J. Numer. Methods Fluids 71 (9) (2013) 1178–1190.
[44] D. Kuzmin, Hierarchical slope limiting in explicit and implicit discontinuous Galerkin methods, J. Comput. Phys. 257 (2014) 1140–1162.
[45] V. Dolejsi, M. Feistauer, C. Schwab, On some aspects of the discontinuous Galerkin finite element method for conservation laws, Math. Comput. Simul. 61 (3–6) (2003) 333–346.
[46] M. Dubiner, Spectral methods on triangles and other domains, J. Sci. Comput. 6 (1991) 345–390.
[47] M. Dumbser, D. Balsara, E.F. Toro, C.D. Munz, A unified framework for the construction of one-step finite-volume and discontinuous Galerkin schemes, J. Comput. Phys. 227 (2008) 8209–8253.

[48] M. Dumbser, D.S. Balsara, A new, efficient formulation of the HLLEM Riemann solver for general conservative and non-conservative hyperbolic systems, J. Comput. Phys. 304 (2016) 275–319.
[49] M. Dumbser, W. Boscheri, High-order unstructured Lagrangian one-step WENO finite volume schemes for non-conservative hyperbolic systems: applications to compressible multi-phase flows, Comput. Fluids 86 (2013) 405–432.
[50] M. Dumbser, M. Castro, C. Parés, E.F. Toro, ADER schemes on unstructured meshes for non-conservative hyperbolic systems: applications to geophysical flows, Comput. Fluids 38 (2009) 1731–1748.
[51] M. Dumbser, C. Enaux, E.F. Toro, Finite volume schemes of very high order of accuracy for stiff hyperbolic balance laws, J. Comput. Phys. 227 (2008) 3971–4001.
[52] M. Dumbser, A. Hidalgo, M. Castro, C. Parés, E.F. Toro, FORCE schemes on unstructured meshes II: non-conservative hyperbolic systems, Comput. Methods Appl. Mech. Eng. 199 (2010) 625–647.
[53] M. Dumbser, A. Hidalgo, O. Zanotti, High order space-time adaptive ADER-WENO finite volume schemes for non-conservative hyperbolic systems, Comput. Methods Appl. Mech. Eng. 268 (2014) 359–387.
[54] M. Dumbser, M. Käser, Arbitrary high order non-oscillatory finite volume schemes on unstructured meshes for linear hyperbolic systems, J. Comput. Phys. 221 (2007) 693–723.
[55] M. Dumbser, M. Käser, V.A. Titarev, E.F. Toro, Quadrature-free non-oscillatory finite volume schemes on unstructured meshes for nonlinear hyperbolic systems, J. Comput. Phys. 226 (2007) 204–243.
[56] M. Dumbser, C.D. Munz, Building blocks for arbitrary high order discontinuous Galerkin schemes, J. Sci. Comput. 27 (2006) 215–230.
[57] M. Dumbser, T. Schwartzkopff, C.D. Munz, Arbitrary high order finite volume schemes for linear wave propagation, in: Computational Science and High Performance Computing II, in: Notes on Numerical Fluid Mechanics and Multidisciplinary Design, Springer, 2006, pp. 129–144.
[58] M. Dumbser, E.F. Toro, On universal Osher-type schemes for general nonlinear hyperbolic conservation laws, Commun. Comput. Phys. 10 (2011) 635–671.
[59] M. Dumbser, E.F. Toro, A simple extension of the Osher Riemann solver to non-conservative hyperbolic systems, J. Sci. Comput. 48 (2011) 70–88.
[60] M. Dumbser, O. Zanotti, Very high order PNPM schemes on unstructured meshes for the resistive relativistic MHD equations, J. Comput. Phys. 228 (2009) 6991–7006.
[61] M. Dumbser, O. Zanotti, A. Hidalgo, D.S. Balsara, ADER-WENO finite volume schemes with space-time adaptive mesh refinement, J. Comput. Phys. 248 (2013) 257–286.
[62] M. Dumbser, O. Zanotti, R. Loubère, S. Diot, A posteriori subcell limiting of the discontinuous Galerkin finite element method for hyperbolic conservation laws, J. Comput. Phys. 278 (December 2014) 47–75.
[63] B. Einfeldt, On Godunov-type methods for gas dynamics, SIAM J. Numer. Anal. 25 (1988) 294–318.
[64] B. Einfeldt, C.D. Munz, P.L. Roe, B. Sjögreen, On Godunov-type methods near low densities, J. Comput. Phys. 92 (1991) 273–295.
[65] S. Fechter, C.D. Munz, A discontinuous Galerkin based sharp-interface method to simulate three-dimensional compressible two-phase flow, Int. J. Numer. Methods Fluids 78 (2015) 413–435.
[66] M. Feistauer, V. Kucera, K. Najzar, J. Prokopová, Analysis of space-time discontinuous Galerkin method for nonlinear convection–diffusion problems, Numer. Math. 117 (2) (2011) 251–288.
[67] T. Gardiner, J.M. Stone, An unsplit Godunov method for ideal MHD via constrained transport, J. Comput. Phys. 205 (2005) 509–539.
[68] T. Gardiner, J.M. Stone, An unsplit Godunov method for ideal MHD via constrained transport in three dimensions, J. Comput. Phys. 227 (2008) 4123–4141.
[69] G. Gassner, M. Dumbser, F. Hindenlang, C.D. Munz, Explicit one-step time discretizations for discontinuous Galerkin and finite volume schemes based on local predictors, J. Comput. Phys. 230 (2011) 4232–4247.
[70] G. Gassner, F. Lörcher, C.D. Munz, A discontinuous Galerkin scheme based on a space-time expansion II. Viscous flow equations in multi dimensions, J. Sci. Comput. 34 (2008) 260–286.
[71] S.K. Godunov, Finite difference methods for the computation of discontinuous solutions of the equations of fluid dynamics, Math. USSR Sb. 47 (1959) 271–306.
[72] S. Gottlieb, C.W. Shu, Total variation diminishing Runge–Kutta schemes, Math. Comput. 67 (1998) 73–85.
[73] A. Harten, B. Engquist, S. Osher, S. Chakravarthy, Uniformly high order essentially non-oscillatory schemes, III, J. Comput. Phys. 71 (1987) 231–303.
[74] J.S. Hesthaven, T. Warburton, Nodal Discontinuous Galerkin Methods: Algorithms Analysis and Applications, Springer, New York, 2008.
[75] A. Hidalgo, M. Dumbser, ADER schemes for nonlinear systems of stiff advection–diffusion–reaction equations, J. Sci. Comput. 48 (2011) 173–189.
[76] H. Luo, J.D. Baum, R. Löhner, A Hermite WENO-based limiter for discontinuous Galerkin method on unstructured grids, J. Comput. Phys. 225 (1) (July 2007) 686–713.
[77] S. Hou, X.D. Liu, Solutions of multi-dimensional hyperbolic systems of conservation laws by square entropy condition satisfying discontinuous Galerkin method, J. Sci. Comput. 31 (2007) 127–151.
[78] C. Hu, C.W. Shu, Weighted essentially non-oscillatory schemes on triangular meshes, J. Comput. Phys. 150 (1999) 97–127.
[79] X.Y. Hu, N.A. Adams, C.W. Shu, Positivity-preserving method for high-order conservative schemes solving compressible Euler equations, J. Comput. Phys. 242 (2013) 169–180.
[80] A. Huerta, E. Casoni, J. Peraire, A simple shock-capturing technique for high-order discontinuous Galerkin methods, Int. J. Numer. Methods Fluids 69 (10) (2012) 1614–1632.
[81] G. Jiang, C.W. Shu, On a cell entropy inequality for discontinuous Galerkin methods, Math. Comput. 62 (1994) 531–538.
[82] G.S. Jiang, C.C. Wu, A high-order WENO finite difference scheme for the equations of ideal magnetohydrodynamics, J. Comput. Phys. 150 (1999) 561–594.
[83] J. Qiu, C-W. Shu, Hermite WENO schemes and their application as limiters for Runge–Kutta discontinuous Galerkin method: one-dimensional case, J. Comput. Phys. 193 (1) (January 2004) 115–135.
[84] J. Qiu, C-W. Shu, A comparison of troubled-cell indicators for Runge–Kutta discontinuous Galerkin methods using weighted essentially nonoscillatory limiters, SIAM J. Sci. Comput. 27 (3) (October 2005) 995–1013.
[85] J.S. Baehr, A priori and a posteriori, http://www.iep.utm.edu/apriori, July 2015.
[86] J. Zhu, J. Qiu, Hermite WENO schemes and their application as limiters for Runge–Kutta discontinuous Galerkin method, III: unstructured meshes, J. Sci. Comput. 39 (2) (May 2009) 293–321.
[87] J. Zhu, J. Qiu, C.W. Shu, M. Dumbser, Runge–Kutta discontinuous Galerkin method using WENO limiters II: unstructured meshes, J. Comput. Phys. 227 (9) (April 2008) 4330–4353.
[88] A.K. Kapila, R. Menikoff, J.B. Bdzil, S.F. Son, D.S. Stewart, Two-phase modelling of DDT in granular materials: reduced equations, Phys. Fluids 13 (2001) 3002–3024.
[89] G.E. Karniadakis, S.J. Sherwin, Spectral/hp Element Methods in CFD, Oxford University Press, 1999.
[90] F. Kemm, On the origin of divergence errors in MHD simulations and consequences for numerical schemes, Commun. Appl. Math. Comput. Sci. 8 (1) (2013) 1–38.
[91] F. Kemm, Roe-type schemes for shallow water magnetohydrodynamics with hyperbolic divergence cleaning, Appl. Math. Comput. 272 (2016) 385–402.

[92] C. Klaij, J.J.W. Van der Vegt, H. Van der Ven, Space-time discontinuous Galerkin method for the compressible Navier–Stokes equations, J. Comput. Phys. 217 (2006) 589–611.
[93] L. Krivodonova, M. Berger, High-order accurate implementation of solid wall boundary conditions in curved geometries, J. Comput. Phys. 211 (2006) 492–512.
[94] L. Krivodonova, J. Xin, J.-F. Remacle, N. Chevaugeon, J.E. Flaherty, Shock detection and limiting with discontinuous Galerkin methods for hyperbolic conservation laws, in: Workshop on Innovative Time Integrators for PDEs, Appl. Numer. Math. 48 (3–4) (2004) 323–338.
[95] A. Kurganov, G. Petrova, B. Popov, Adaptive semidiscrete central-upwind schemes for nonconvex hyperbolic conservation laws, SIAM J. Sci. Comput. 29 (2007) 2381–2401.
[96] Y. Liu, M. Vinokur, Z.J. Wang, Spectral (finite) volume method for conservation laws on unstructured grids V: extension to three-dimensional systems, J. Comput. Phys. 212 (2006) 454–472.
[97] L. Krivodonova, Limiters for high-order discontinuous Galerkin methods, J. Comput. Phys. 226 (September 2007) 879–896.
[98] F. Lörcher, G. Gassner, C.D. Munz, A discontinuous Galerkin scheme based on a space-time expansion. I. Inviscid compressible flow in one space dimension, J. Sci. Comput. 32 (2007) 175–199.
[99] R. Loubère, Contribution to Lagrangian and arbitrary-Lagrangian–Eulerian numerical schemes, PhD thesis, University of Toulouse, France, 2013. Habilitation à diriger des recherches.
[100] R. Loubère, M. Dumbser, S. Diot, A new family of high order unstructured MOOD and ADER finite volume schemes for multidimensional systems of hyperbolic conservation laws, Commun. Comput. Phys. 16 (2014) 718–763.
[101] M. Yang, Z.J. Wang, A parameter-free generalized moment limiter for high-order methods on unstructured grids, in: 47th AIAA Aerospace Sciences Meeting Including the New Horizons Forum and Aerospace Exposition, AIAA 2009-605, http://dx.doi.org/10.2514/6.2009-605.
[102] G. Dal Maso, P.G. LeFloch, F. Murat, Definition and weak stability of nonconservative products, J. Math. Pures Appl. 74 (1995) 483–548.
[103] A. Meister, S. Ortleb, A positivity preserving and well-balanced DG scheme using finite volume subcells in almost dry regions, Appl. Math. Comput. 272 (2016) 259–273.
[104] L.O. Müller, C. Parés, E.F. Toro, Well-balanced high-order numerical schemes for one-dimensional blood flow in vessels with varying mechanical properties, J. Comput. Phys. 242 (2013) 53–85.
[105] L.O. Müller, E.F. Toro, Well-balanced high-order solver for blood flow in networks of vessels with variable properties, Int. J. Numer. Methods Biomed. Eng. 29 (12) (2013) 1388–1411.
[106] A. Murrone, H. Guillard, A five equation reduced model for compressible two phase flow problems, J. Comput. Phys. 202 (2005) 664–698.
[107] J. Von Neumann, R.D. Richtmyer, A method for the numerical calculation of hydrodynamic shocks, J. Appl. Phys. 21 (1950) 232–237.
[108] S.A. Orszag, C.M. Tang, Small-scale structure of two-dimensional magnetohydrodynamic turbulence, J. Fluid Mech. 90 (1979) 129.
[109] C. Parés, Numerical methods for nonconservative hyperbolic systems: a theoretical framework, SIAM J. Numer. Anal. 44 (2006) 300–321.
[110] P.O. Persson, J. Peraire, Sub-cell shock capturing for discontinuous Galerkin methods, AIAA Paper 2006-112, 2006.
[111] J.M. Picone, R.B. Dahlburg, Evolution of the Orszag–Tang vortex system in a compressible medium. II. Supersonic flow, Phys. Fluids B 3 (1991) 29–44.
[112] J. Qiu, M. Dumbser, C.W. Shu, The discontinuous Galerkin method with Lax–Wendroff type time discretizations, Comput. Methods Appl. Mech. Eng. 194 (2005) 4528–4543.
[113] J. Qiu, C.W. Shu, Hermite WENO schemes and their application as limiters for Runge–Kutta discontinuous Galerkin method: one-dimensional case, J. Comput. Phys. 193 (2003) 115–135.
[114] J. Qiu, C.W. Shu, Hermite WENO schemes and their application as limiters for Runge–Kutta discontinuous Galerkin method II: two dimensional case, Comput. Fluids 34 (2005) 642–663.
[115] J. Qiu, C.W. Shu, Runge–Kutta discontinuous Galerkin method using WENO limiters, SIAM J. Sci. Comput. 26 (2005) 907–929.
[116] R. Biswas, K.D. Devine, J.E. Flaherty, Parallel, adaptive finite element methods for conservation laws, Appl. Numer. Math. 14 (1994) 255–283.
[117] W.H. Reed, T.R. Hill, Triangular mesh methods for neutron transport equation, Technical Report LA-UR-73-479, Los Alamos Scientific Laboratory, 1973.
[118] R. Hartmann, P. Houston, Adaptive discontinuous Galerkin finite element methods for the compressible Euler equations, J. Comput. Phys. 183 (2) (2002) 508–532.
[119] S. Rhebergen, O. Bokhove, J.J.W. van der Vegt, Discontinuous Galerkin finite element methods for hyperbolic nonconservative partial differential equations, J. Comput. Phys. 227 (2008) 1887–1922.
[120] V.V. Rusanov, Calculation of interaction of non-steady shock waves with obstacles, J. Comput. Math. Phys. USSR 1 (1961) 267–279.
[121] R. Saurel, R. Abgrall, A multiphase Godunov method for compressible multifluid and multiphase flows, J. Comput. Phys. 150 (1999) 425–467.
[122] R. Saurel, R. Abgrall, A simple method for compressible multifluid flows, SIAM J. Sci. Comput. 21 (1999) 1115–1145.
[123] T. Schwartzkopff, C.D. Munz, E.F. Toro, ADER: a high order approach for linear hyperbolic systems in 2D, J. Sci. Comput. 17 (1–4) (2002) 231–240.
[124] D.W. Schwendeman, C.W. Wahle, A.K. Kapila, The Riemann problem and a high-resolution Godunov method for a model of compressible two-phase flow, J. Comput. Phys. 212 (2006) 490–526.
[125] C.W. Shu, S. Osher, Efficient implementation of essentially non-oscillatory shock capturing schemes, J. Comput. Phys. 77 (1988) 439–471.
[126] C.W. Shu, S. Osher, Efficient implementation of essentially non-oscillatory shock capturing schemes II, J. Comput. Phys. 83 (1989) 32–78.
[127] G.A. Sod, A survey of several finite difference methods for systems of non-linear hyperbolic conservation laws, J. Comput. Phys. 27 (1978) 1–31.
[128] M. Sonntag, C.D. Munz, Shock capturing for discontinuous Galerkin methods using finite volume subcells, in: J. Fuhrmann, M. Ohlberger, C. Rohde (Eds.), Finite Volumes for Complex Applications VII, Springer, 2014, pp. 945–953.
[129] A. Taube, M. Dumbser, D. Balsara, C.D. Munz, Arbitrary high order discontinuous Galerkin schemes for the magnetohydrodynamic equations, J. Sci. Comput. 30 (2007) 441–464.
[130] V.A. Titarev, E.F. Toro, ADER: arbitrary high order Godunov approach, J. Sci. Comput. 17 (1–4) (December 2002) 609–618.
[131] V.A. Titarev, E.F. Toro, ADER schemes for three-dimensional nonlinear hyperbolic systems, J. Comput. Phys. 204 (2005) 715–736.
[132] E.F. Toro, V.A. Titarev, Derivative Riemann solvers for systems of conservation laws and ADER methods, J. Comput. Phys. 212 (1) (2006) 150–165.
[133] E.F. Toro, Riemann Solvers and Numerical Methods for Fluid Dynamics, third edition, Springer, 2009.
[134] E.F. Toro, V.A. Titarev, Solution of the generalized Riemann problem for advection–reaction equations, Proc. R. Soc. Lond. (2002) 271–281.
[135] J.J.W. van der Vegt, H. van der Ven, Space-time discontinuous Galerkin finite element method with dynamic grid motion for inviscid compressible flows I. General formulation, J. Comput. Phys. 182 (2002) 546–585.
[136] H. van der Ven, J.J.W. van der Vegt, Space-time discontinuous Galerkin finite element method with dynamic grid motion for inviscid compressible flows II. Efficient flux quadrature, Comput. Methods Appl. Mech. Eng. 191 (2002) 4747–4780.
[137] M.J. Vuik, J.K. Ryan, Automated parameters for troubled-cell indicators using outlier detection, SIAM J. Sci. Comput. 38 (1) (2016) A84–A104.
[138] Z.J. Wang, Adaptive High-Order Methods in Computational Fluid Dynamics, Advances in Computational Fluid Dynamics, World Scientific, 2011.
[139] Z.J. Wang, L. Zhang, Y. Liu, Spectral (finite) volume method for conservation laws on unstructured grids IV: extension to two-dimensional Euler equations, J. Comput. Phys. 194 (2004) 716–741.
[140] P. Woodward, P. Colella, The numerical simulation of two-dimensional fluid flow with strong shocks, J. Comput. Phys. 54 (1984) 115–173.
[141] M. Yang, Z. Wang, A parameter-free generalized moment limiter for high-order methods on unstructured grids, Adv. Appl. Math. Mech. (2009).
[142] O. Zanotti, F. Fambri, M. Dumbser, Solving the relativistic magnetohydrodynamics equations with ADER discontinuous Galerkin methods, a posteriori subcell limiting and adaptive mesh refinement, Mon. Not. R. Astron. Soc. 452 (2015) 3010–3029.

[143] O. Zanotti, F. Fambri, M. Dumbser, A. Hidalgo, Space-time adaptive ADER discontinuous Galerkin finite element schemes with a posteriori subcell finite volume limiting, Comput. Fluids 118 (2015) 204–224.
[144] X. Zhang, C.W. Shu, On positivity-preserving high order discontinuous Galerkin schemes for compressible Euler equations on rectangular meshes, J. Comput. Phys. 229 (2010) 8918–8934.
[145] X. Zhang, C.W. Shu, Positivity-preserving high order finite difference WENO schemes for compressible Euler equations, J. Comput. Phys. 231 (2012) 2245–2258.
[146] X. Zhong, C.W. Shu, A simple weighted essentially nonoscillatory limiter for Runge–Kutta discontinuous Galerkin methods, J. Comput. Phys. 232 (1) (January 2013) 397–415.
[147] J. Zhu, J. Qiu, Runge–Kutta discontinuous Galerkin method using WENO type limiters: three dimensional unstructured meshes, Commun. Comput. Phys. (2012) 985–1005.
[148] J. Zhu, X. Zhong, C.W. Shu, J. Qiu, Runge–Kutta discontinuous Galerkin method using a new type of WENO limiters on unstructured meshes, J. Comput. Phys. 248 (2013) 200–220.